arXiv:1611.06311v1 [astro-ph.HE] 19 Nov 2016

Understanding the General Feature of Microvariability in *Kepler* Blazar W2R 1926+42

Mahito SASADA[1,2], Shin MINESHIGE[2], Shinya YAMADA[3] and Hitoshi NEGORO[4]

[1]Institute for Astrophysical Research, Boston University, 725 Commonwealth Avenue, Boston, MA 02215, USA

[2]Department of Astronomy, Graduate School of Science, Kyoto University, Kitashirakawa-Oiwake-cho, Sakyo-ku, Kyoto 606-8502, Japan

[3]Department of Physics, Tokyo Metropolitan University, Minami-Osawa 1-1 Hachioji, Tokyo 192-0397, Japan

[4]Department of Physics, Nihon University, 1-8 Kanda-Surugadai, Chiyoda-ku, Tokyo 101-8308, Japan

*E-mail: sasada@bu.edu

Received 2016 January 26; Accepted 2016 November 13

Abstract

We analyze the *Kepler* monitoring light curve of a blazar W2R 1926+42 to examine features of microvariability by means of the "shot analysis" technique. We select 195 intra-day, flare-like variations (shots) for the continuous light curve of Quarter 14 with a duration of 100 d. In the application of the shot analysis, an averaged profile of variations is assumed to converge with a universal profile which reflects a physical mechanism generating the microvariability in a blazar jet, although light-variation profiles of selected shots show a variety. A mean profile, which is obtained by aligning the peaks of the 195 shots, is composed of a spiky-shape shot component at $\pm$0.1 d (with respect to the time of the peak), and two slow varying components ranging from $-$0.50 d to $-$0.15 d and from 0.10 d to 0.45 d of the peak time. The former spiky feature is well represented by an exponential rise of 0.043$\pm$0.001 d and an exponential decay of 0.061$\pm$0.002 d. These timescales are consistent with that corresponding to a break frequency of a power spectrum density calculated from the obtained light curve. After verification with

the Monte-Carlo method, the exponential shape, but not the observed asymmetry, of the shot component can be explained by noise variation. The asymmetry is difficult to explain through a geometrical effect (i.e. changes of the geometry of the emitting region), but is more likely to be caused by the production and dissipation of high-energy accelerated particles in the jet. Additionally, durations of the detected shots show a systematic variation with a dispersion caused by a statistical randomness. A comparison with the variability of Cygnus X-1 is also briefly discussed.

Key words: galaxies: active - galaxies: jets - galaxies: individual (W2R 1926+42) - techniques: photometric - methods: observational

1 Introduction

Blazars have relativistic jets whose axes are nearly aligned to the line of sight (Blandford & Königl 1979; Antonucci 1993). In principle, timescales of brightness variations in blazars are related to sizes of emitting regions and the speeds of motions in relativistic jets. Variations, however, have a variety of timescales ranging from minutes to decades. The power spectrum density (PSD) of a blazar can be fit by a power law, which means that variations of blazars follow a noise-like behavior (Kataoka et al. 2001). Brightness variations of blazars could be affected by a variety of physical conditions: size and speed of the emission region, changes in magnetic field, etc. Shorter-timescale variations can reflect physical processes in the inner emitting regions of a jet without any direct relation to the other, more slowly varying component(s). The study of short-timescale fluctuations is therefore important toward investigation of the origin of variation in blazar jets.

Blazars show variations having a timescale of less than one day, termed ”microvariability”. Such microvariability has been reported over wide ranges of wavelengths from radio (Quirrenbach et al. 1992), to optical (Carini et al. 1990), X-ray (Kataoka et al. 2001), and TeV bands (Aharonian et al. 2007). The *Fermi* space telescope scans the entire γ-ray sky every three hours, and has detected flares, large-amplitude variations, in a number of blazars (Abdo et al. 2011). Saito et al. (2013) reported that a few flares in PKS 1510$-$089 exhibited asymmetric profiles. Nalewajko (2013), however, reported that there was a great variety of flare shapes and duration among 40 flares that he studied, so that the flares cannot be described by a simple rise and decay. It is not easy to extract detailed features of flare-like variations in the γ-ray band, because the time required to measure the γ-ray flux with *Fermi* and *AGILE* is usually longer than 3 hours (in the exceptional case of minutes-timescale

γ-ray variation in 3C 279 reported by Ackermann et al. 2016), since the number of detected photons is limited. A statistical study of a sizeable number of variation events with higher time resolution and with good photon statistics is needed to extract the general features of microvariability in an effort to understand the underlying physics of relativistic jets.

The blazar W2R 1926+42 has a synchrotron spectral energy distribution (SED) that peaks at a frequency of below 10^{13} Hz. The object is classified as a low-frequency peaked BL Lac object at a redshift $z = 0.154$ that is estimated from two absorption lines in the spectrum of its host galaxy (Edelson & Malkan 2012). Edelson et al. (2013) also reported numerous flares on timescales as short as 1 day in the *Kepler* light curve with 30-minute time sampling in Quarters 11 and 12. Continuous optical monitoring of W2R 1926+42 with denser (1 minute) time sampling by *Kepler* (Borucki et al. 2010) in Quarter 14 detected considerable microvariability of the flux.

We wish to stress here that it is of limited use to examine a variety of individual shapes of the time profiles of flux variations. In order to gain physical insight, it is more useful to examine the average properties. Therefore, in this paper we adopt a stacking analysis, so-called "shot analysis", to obtain a mean profile of rapid variations. The paper is organized as follows. Details of the *Kepler* observed light curve and its PSD are described in §2. The methods of time series analysis, shot analysis, bootstrap method, and Monte-Carlo method, are described in §3. Observational features of the mean profile of rapid variations and its validation by a Mote-Carlo simulation are reported in §4. We then discuss the mechanism of variations as derived from general features of the rapid fluctuations in §5. Several concluding remarks based on our results are provided in §6.

2 Observation and Light curve

2.1 *Kepler* Data

Kepler monitored over a 100,000 objects in the Cygnus region, obtaining continuous light curves with two timing settings, long (30-minute) and short (1-minute) integrations. W2R 1926+42 is listed in the *Kepler* target list. A continuous light curve with the long cadence has been obtained since Quarter 11. In Quarter 14, the object was monitored in the short cadence mode for 100 d. We have produced the calibrated "SAP_FLUX" light curve with 1-minute time resolution by the automated *Kepler* data processing pipeline (Jenkins et al. 2010).

2.2 Light Curve

Figure 1 shows an optical light curve of the object obtained by *Kepler*. The blazar displayed violent variability over various timescales ranging from several tens of minutes to over 10 days during this

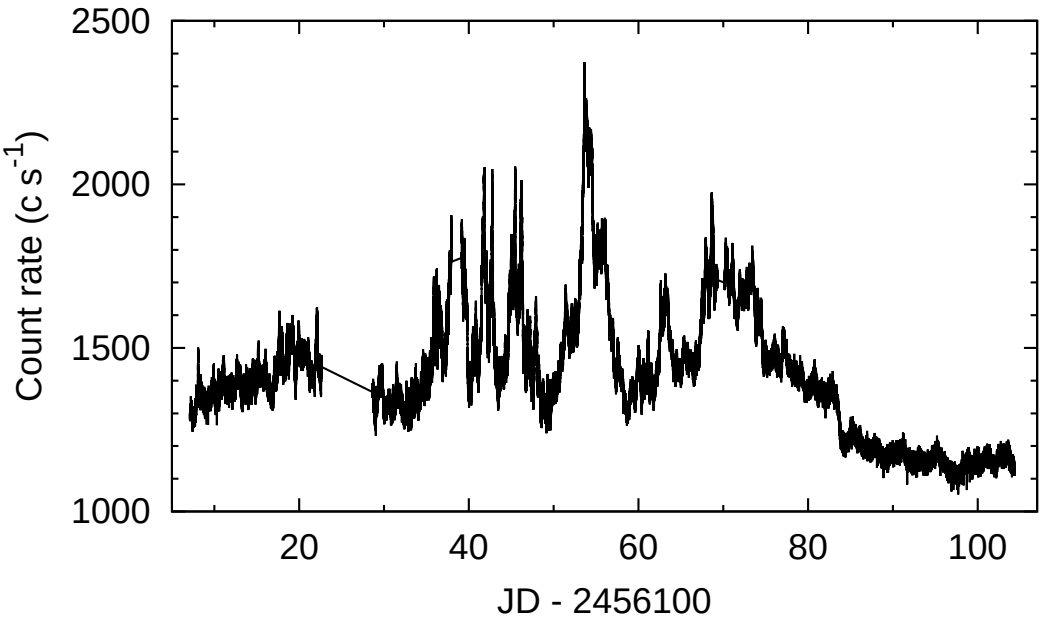

Fig. 1. Light curve obtained by the *Kepler* spacecraft over the entire Quarter 14 period. The object was monitored for 100 d with 1-minute time resolution.

monitoring. The light curve is composed of not only large-amplitude, long-term variations such as that ranging from JD 2456150 to 2456160, but also numerous flare-like variations with timescales < 1 d. These rapid variations exist throughout this entire monitoring period. A variety of profiles is apparent in these rapid variations. Figure 12 shows all profiles of the detected rapid variations.

2.3 Power Spectrum Density

Power spectrum density (PSD) analysis is one of the best ways to quantify time-series data. We calculate the PSD of the *Kepler* light curve to explore whether there is a characteristic timescale or not. We separate the observed light curve into five epochs, each with a duration of approximately 20 d, and calculate PSDs at each epoch. In doing so, we implicitly assume that the PSD is stationary throughout the entire range of the light curve. We average 20 continuos power estimates and calculate the standard error on a logarithmic scale (Papadakis & Lawrence 1993). The standard error would contain the systematic one affected by the variation of PSDs in each epoch.

Figure 2 shows the PSDs calculated from the observed light curve. We calculate the best-fit power-law function, adding a constant value in panel (A), by evaluating the goodness-of-fit with a χ^2 test;

$$\chi^2 = \sum \left(\frac{P_{\rm obs} - P_{\rm expect}}{\sigma_{\rm err}} \right)^2, \tag{1}$$

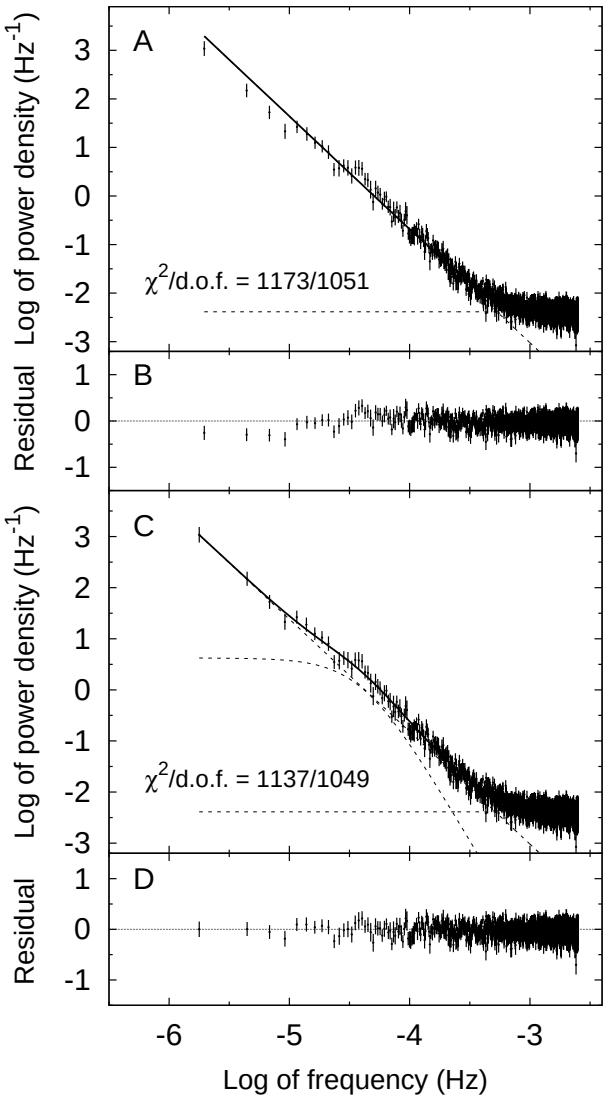

Fig. 2. Power spectrum densities calculated from the observed light curve. Panels (A) and (B) show the observed PSD, the best-fit power-law function and constant, and its residuals. Panels (C) and (D) show the PSD, the best-fit function of (2), and its residuals. Dashed lines in panel (A) and (C) show individual components of the best-fit functions. Goodnesses of fit, χ^2 per degrees of freedom (d.o.f), are also indicated.

where $P_{\rm obs}$ and $P_{\rm expect}$ are observed and expected PSDs, and $\sigma_{\rm err}$ is the uncertainty in the observed PSD. Residuals in panel (B) indicate a discrepancy at lower frequencies. We add a squared Lorentzian component to the power-law function as;

$$P_{\rm model}(f) = A\, f^{-\alpha} + \frac{B}{[1+(f/f_{\rm br})^2]^2} + C, \tag{2}$$

where α is a spectral index and $f_{\rm br}$ is a break frequency. The best-fit function is shown in panel (C). Dashed lines represent individual terms of function (2). The goodness of fit for the best-fit function improves over that for the best-fit power law. The existence of this curvature has already been pointed out (Edelson et al. 2013; Mohan et al. 2016).

The curvature in the observed PSD indicates that the light curve has the characteristic timescale related to the break frequency of the PSD. The break frequency of the best-fit function (2) is $4.1^{+0.6}_{-0.5}\times10^{-5}$ Hz, corresponding to $f_{\rm br} = (2\pi\tau_{\rm br})^{-1}$, with $\tau_{\rm br} = 0.045 \pm 0.006$ d, for time-symmetry exponential shots (Negoro et al. 2001).

If the variation is caused by flickering or 1/f fluctuation, there is no physical significance in the rapid variation associated with the higher-frequency PSD component, because a higher-frequency variation is generated as a result of a longer-timescale fluctuation. This fluctuation, however, should not have a characteristic timescale. The observed characteristic timescale indicates the underlying physics associated with that timescale.

3 Time Series Analysis Techniques

3.1 Shot Analysis

Frequency-domain (e.g. PSD) analyses are easy to perform, but are difficult to relate to physical mechanisms. One would prefer a time-domain study that is useful for investigating the physical mechanisms of flare-like variations. This is, however, not easy to accomplish, especially when the photon statistics are insufficient, because it is difficult to perform detailed studies on a section of the observed data with high observational uncertainties. Additionally, observed flares in blazars usually have a variety of shapes (Nalewajko 2013). Thus, it is difficult to extract common features of blazar flare-like variations by studying only individual events.

Shot analysis proposed by Negoro et al. (1994) is one of the best way to study the common features of variation. The shot analysis calculate the mean of flare-like variation events by stacking these events. This mean can be reduced the influence of the variety of shapes at individual events as well as the variations caused by the observational uncertainty. Here, the averaged profile of flare-like variations is assumed to converge with a universal one. In other words, if samples of flare-like variations are innumerable, its average profile should be coincident with the universal one reflecting

general features of flare-like variations. If the variability has the characteristic timescale, the phase information can be extracted from the mean profile of the variations associated with the characteristic timescale, regardless of whether the variability ascribes continuous or discrete processes. Hence we can investigate the physical mechanism associated with the characteristic-timescale variation from the mean of flare-like variation events.

We apply the shot analysis to the light curve of W2R 1926+42 obtained by *Kepler* in order to generate a mean profile of flare-like rapid variations and to study its general features without being distracted by features specific to individual events. We adopt the following procedures to select rapid variations.

1. Estimate the observational uncertainty in the light curve
2. Select rapid variations from the light curve as representatives of flaring events
3. Approximate a long-term slow-varying component with a polynomial function in each candidate
4. After subtracting the long-term components, select the rapid variations with variation amplitudes that are four times larger than the observational uncertainty

We define these representative variations as shots. After identifying the shots, we stack them aligning their peaks, and calculate the mean profile. An example of shot detection is shown in §4.1.1.

The observational uncertainty is estimated as follows. There are two possibilities for varying the observed brightness: intrinsic variation of the object and variation from observational uncertainty. The latter can be dominant over the former within a short time period. We calculate differences of fluxes between two neighboring points as, $\Delta F(t_n) = F(t_{n+1}) - F(t_n)$, where $F(t_{n+1})$ and $F(t_n)$ are the $(n+1)$-th and n-th photon fluxes at those times. We define the standard deviation σ of $\Delta F(t_n)$ as the observational uncertainty, σ =17.15 count s^{-1}. At this time, we do not include values of $\Delta F(t_n)$ with long time differences (> 2 min) to avoid contaminations of data that might have components with large intrinsic variations because the light curve often has long blank periods caused by instrumental limitations.

Rapid variations are often superposed on long-term variations in the light curves of blazars (Sasada et al. 2008). We approximate the long-term baseline component by a second-order local polynomial that fits the trend of the light curve when the rapid fluctuations are ignored. We identify a shot when the estimated amplitude of the rapid variation, without the contribution of the baseline component, is larger than our threshold criterion, $>4\sigma$.

The peak time of the shot is defined as the time of maximum flux in the light curve after subtraction of the baseline component. We calculate the mean profile of detected shots by stacking numerous shots after aligning their peaks. Here, we average the shots without subtracting the baseline

components. The final shape of the mean profile does not depend on the existence of the baseline component in each shot, since the baseline component of the mean profile should be smoothed and asymptotically close to constant in time.

3.2 Non-parametric Bootstrap Method

The bootstrap method that we employ determines the distribution of an estimator or test statistic by resampling either the data or a model derived from the data (Efron & Tibshirani 1979; Efron 1994). The bootstrap method first provides an approximation to the probability distribution of the estimator in the detected samples. Then, the coverage probabilities of confidence intervals can be estimated from the probabilities of the distributions. We apply a non-parametric bootstrap method to the dataset of shots, and try to estimate a systematic uncertainty and a confidence interval of the mean profile of shots, as well as confidence intervals of best-fit parameters of the function that reproduce the mean profile of resampled shots.

We identify 195 shots from the *Kepler* monitoring light curve of W2R 1926+42, as presented below in §4.1. We resample these shots to produce 195 resampled shots. We then calculate the mean profile using these resampled shots (hereafter, resampled mean profile). We produce 10^4 resampled mean profiles with different resamplings by following this procedure.

The best-fit parameters of the function representing the shots can be calculated from each resampled mean profile. Confidence intervals of parameters of the function can be evaluated from the probability distributions of the best-fit parameters calculated from each resampled mean profile.

3.3 Monte-Carlo Simulation of Noise Variation

Time-series analyses in past studies have found that blazar variations are similar to aperiodic red noise, meaning that variations on longer timescales have greater power. We evaluate the characteristics of noise process by applying the above shot analysis. We then compare the characteristics with the observed features of the mean profile of shots, and examine the difference between the shot features estimated from the noise process and the observed light curve.

We adopt a Monte-Carlo method that applies the inverse Fourier transform of the observed PSD to represent aperiodic noise-like linear time series with a additive sine model (Timmer & König 1995). At this point, we assume the best-fit model of function (2) when the observed PSD is used as the input. Furthermore, we adopt a generation process of non-linear time series with a multiplicative sine model proposed by Uttley, McHardy & Vaughan (2005). We actually calculate a simulated linear time series by a fast Fourier transform technique, with the PSD including random fluctuations. We

then convert this to a simulated non-linear time series through an exponential transform.

The time resolution of a simulated variation is 60 s, and its duration is 100 d (corresponding to the estimations of 144000 points). The mean and standard deviation, μ_l and σ_l, of the generated simulated linear variation, $l(t)$, is adjusted to that of the observed light curve (equal to 1413.7 count s^{-1} and 197.3 count s^{-1}). To calculate a simulated non-linear variation, $x(t)$, first the generated simulated linear variation is offset to μ_l=0. Next, its variation is converted through an exponential transform. Then the mean and standard deviation of its non-linear variation, μ_x and σ_x, are represented as

$$\mu_x = \exp\left[\frac{1}{2}\sigma_l^2\right], \tag{3}$$

$$\sigma_x = \exp\left[\sigma_l^2\right]\left(\exp\left[\sigma_l^2\right] - 1\right). \tag{4}$$

A fractional rms, $\sigma_{\rm frac}$, is defined as the standard deviation divided by the mean, which corresponds to a skewness of $x(t)$. This fractional rms is characterized by equations (3) and (4) as,

$$\sigma_{\rm frac} = \sqrt{\exp\left[\sigma_l^2\right] - 1}. \tag{5}$$

In this simulation, we assume that $\sigma_{\rm frac}$ of the simulated non-linear variation is equal to 0.64. Finally, the mean and standard deviation of $x(t)$ are adjusted to the observed values.

We select local peaks of the simulated linear variation. Mean profiles of local peaks in the simulated linear and non-linear variations are calculated from 195 peaks, the same as the number of detected shots (see at §4.1.2 below).

4 RESULTS

4.1 Shot Analysis

The PSD analysis reveals that the variability of W2R 1926+42 has the characteristic timescale as the curvature of the PSD. This indicates the physical background associated with the variation timescale. We perform the shot analysis to the *Kepler* light curve to extract phase information of variation with the characteristic timescale of the object.

A large number of hour-scale episodes of rapid variations are detected in the light curve. We generate the mean profile of shots that satisfy the definition mentioned at §3.1 to extract general features of the rapid variation.

4.1.1 Example of Shot Detection

Many temporal surges in flux are seen in the light curve. We select these surges and discriminate against large-amplitude variations according to the criteria given in §3.1. Figure 3 shows an example of shot detection. Only the peak at JD 2456108.09 can be identified as a shot. We estimate the

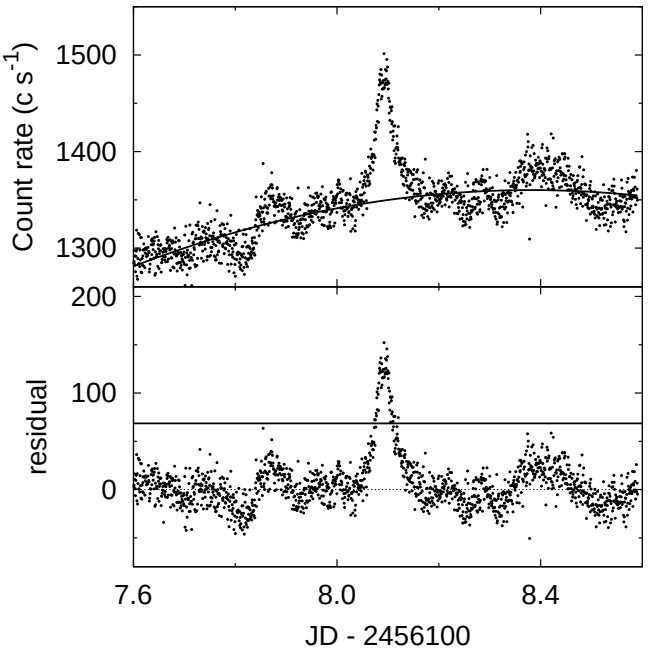

Fig. 3. Example of shot detection. Top panel shows a light curve with a detected shot and a polynomial function approximating a long-term baseline component underlying the shot shown as solid line. Bottom panel shows the light curve after subtraction of the best-fit polynomial function. Solid line indicates the threshold for detecting shots.

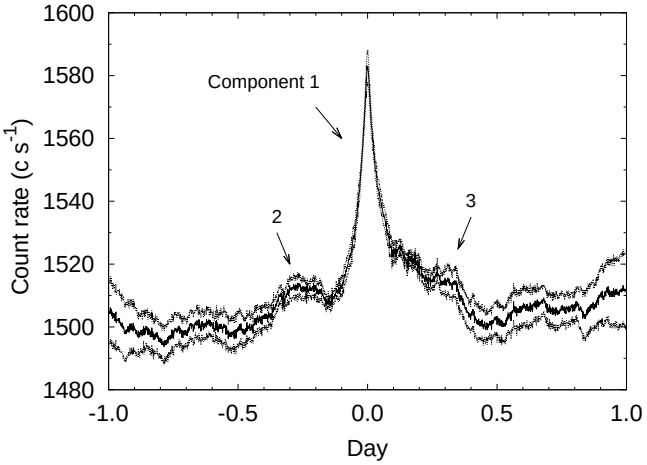

Fig. 4. The mean profile of detected shots. Dotted lines show standard deviations of the mean profile. These standard deviations are calculated from mean profiles of shots detected at light curves which are separated six epochs. See the text for details.

amplitude of the variation by subtracting the best-fit polynomial baseline component of the light curve. Small-amplitude surges seen on JD 2456107.86 and 2456108.40 do not satisfy the criteria of shots. We detect 195 shots from the entire light curve. All shots are displayed in Figure 12.

4.1.2 Mean Profile of Shots

We calculate the mean profile of 195 detected shots. Figure 4 shows the mean profile of shots. The plot omits the count rate at the peak time ($t = 0$), since positive fluctuations of the counts at this time are summed systematically (Negoro et al. 1994).

There are three mainly components at the mean profile: a spike-like component in $\pm$0.1 d (component 1), and slowly varying components ranging from $-$0.50 to $-$0.15 d and from 0.10 to 0.45 d (component 2 and 3, respectively). The increase and decrease of component 1 are well reproduced by an exponential rise and decay. The peak is spiky but smoothly connected from the rise to decay phases.

There is a possibility that shots evolve with time. The systematic uncertainty of the mean profile of shots should include the influence of time evolution of shots. To estimate the systematic uncertainty, we separate the light curve into 6 epochs; (1) JD 2456106–2456125, (2) 2456128.6–2456143.6, (3) 2456143.6–2456158.6, (4) 2456158.6–2456173.6, (5) 2456173.6–2456188.6, and (6) 2456188.6–2456205. Individual mean profiles are calculated from shots located in each epoch. We estimate variances of the mean profiles in each time step. We then calculate the standard deviation of the weighted mean, because the numbers of shots in each epoch are different. Here we normalize fluxes of individual mean profiles within $\pm$1 d to average fluxes over all of the mean profiles, since components 2 and 3 are distributed within $\pm$1 d.

Figure 4 shows the mean profile of shots and calculated standard deviations of the weighted means at each time step. Amplitudes of components 2 and 3 are larger than the standard deviations. Therefore, components 1, 2 and 3 of the mean profile of shots can be regarded as real phenomena, not artifacts of the systematic uncertainty of the sampling of shots.

4.1.3 Model for Component 1 of the Mean Profile

Component 1 is distributed around the peak time of mean profile of shots. General features of shots can be extracted from this component. First, we characterize the shape of component 1 to a function proposed by Abdo et al. (2010):

$$F(t) = F_0 \left[e^{-t/T'_{\rm r}} + e^{t/T'_{\rm d}}\right]^{-1} + F_{\rm c}, \tag{6}$$

where $T'_{\rm r}$ and $T'_{\rm d}$ are variation timescales of the rise and decay phases, $F_{\rm c}$ represents a constant level underlying component 1, and F_0 measures the amplitude of the shot.

We evaluate its goodness-of-fit of this function with a χ^2 test. The standard deviation of the weighted mean between six mean profiles of shots detected from individual epochs is adopted as an estimate of the systematic error, $\sigma_{\rm err}$, to calculate the χ^2 of component 1. The goodness of fit of

component 1 by function (6) is χ^2 =218.7.

In comparison, we apply another function (cf. Negoro et al. 1994):

$$F(t) = \begin{cases} F_0\, e^{|t|/T_{\rm r}} + F_{\rm c}; & (t < 0) \\ F_0\, e^{-|t|/T_{\rm d}} + F_{\rm c}; & (t > 0), \end{cases} \tag{7}$$

where $T_{\rm r}$ and $T_{\rm d}$ are e-folding times of the rise and decay, and $F_{\rm c}$ and F_0 are the same in the case of function (6). Since the number of degrees of freedom is equal to that in the case of function (6), we can compare values of χ^2 between the best-fit functions of (6) and (7) directly. The goodness of fit of function (7) is χ^2=52.6, which is better than that of function (6). Figure 5 shows the applied functions with the best-fit parameters superposed on the mean profile and its residuals. Although function (6) shows obvious residuals during the peak time, as shown in panels (A) and (B) of figure 5, the residuals in the case of function (7) are suppressed, as shown in panels (C) and (D). This indicates that the mean profile is more spiky than expected by function (6). Thus, function (7) is better suited than function (6) to represent the component 1 of the mean profile of shots.

The best-fit parameters of function (7) are shown in table 1. The best-fit e-folding times of the rise and decay phases, at 0.043 d and 0.061 d, are different. We note that the average of these timescales, 0.052$\pm$0.003 d, is consistent with the variation timescale calculated from the break frequency of the PSD within 1-sigma confidence level (§2.3). This result indicates that the component 1 corresponds to the curved feature seen in the observed PSD.

Apparently, the rise timescale of the shot in figure 5 is slightly shorter than that of the decay. Is this difference statistically significant? To answer to this question, we calculate confidence intervals of the parameters of function (7) and the ratio between the rise and decay e-folding times.

We estimate the rise and decay timescales from the best-fit functions (7) of six mean profiles of shots selected from different epochs. The rise and decay timescales are different in epochs; 0.077 and 0.124 (epoch 1), 0.027 and 0.041 (epoch 2), 0.029 and 0.054 (epoch 3), 0.077 and 0.127 (epoch 4), 0.091 and 0.090 (epoch 5), and 0.094 and 0.236 (epoch 6), respectively. These timescales lead that the characteristic timescale is variable in time. We calculate ratios of the rise to decay timescales to understand how asymmetric the mean profiles are. Most of ratios are less than 1, and only one profile is approximately equal to unity. These ratios are distributed from 0.40 to 1.01. We calculate the weighted mean of ratios of timescales and its standard deviation associated with the numbers of shots as 0.63$\pm$0.11. This indicates that the profiles of shots highly tend to show a fast-rise and slow-decay feature.

The mean profile of shots may have a deviation associated with the variation of individual shapes of 195 shots. To verify the effect of this deviation to the asymmetry of the mean profile,

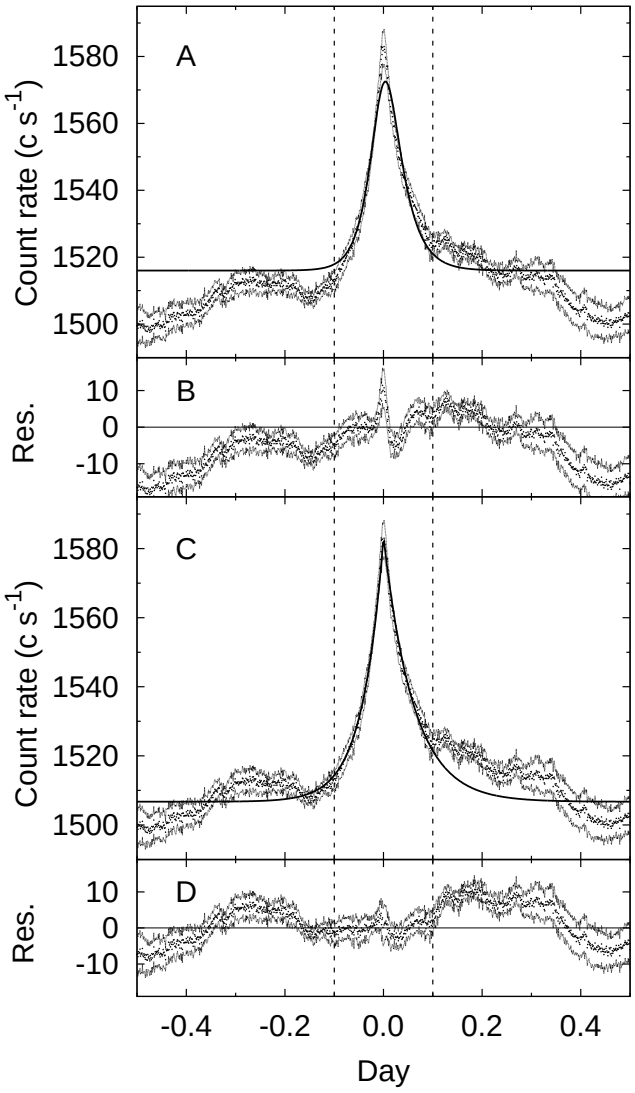

Fig. 5. Best-fit functions superposed on the mean profiles of shots. Panels (A) and (C) show the mean profile of shots and the best-fit functions (6) and (7). Panels (B) and (D) show residuals between the mean profiles and the estimated best-fit functions. Dashed lines show the fitted range.

we evaluate the difference between the rise and decay e-folding times by using the non-parametric bootstrap method as mentioned in §3.2. We generate 10^4 resampled mean profiles, and calculate the best-fit parameters of function (7) for component 1 of each resampled mean profile. The confidence levels of parameters can be estimated from distributions of best-fit parameters. Figure 6 shows distributions of $T_{\rm r}$ and $T_{\rm d}$. This clearly shows that these parameters are differently distributed.

We apply the Wilcoxon rank-sum test which is a non-parametric significance test (also referred to as the Mann-Whitney U-test), to the distributions of $T_{\rm r}$ and $T_{\rm d}$ (Wilcoxon 1945; Mann & Whitney 1947). Since the p value of the Wilcoxon rank-sum test is less than 10^{-15}, we confirm that median values of distributions of $T_{\rm r}$ and $T_{\rm d}$ calculated from the detected shots are clearly different. For these

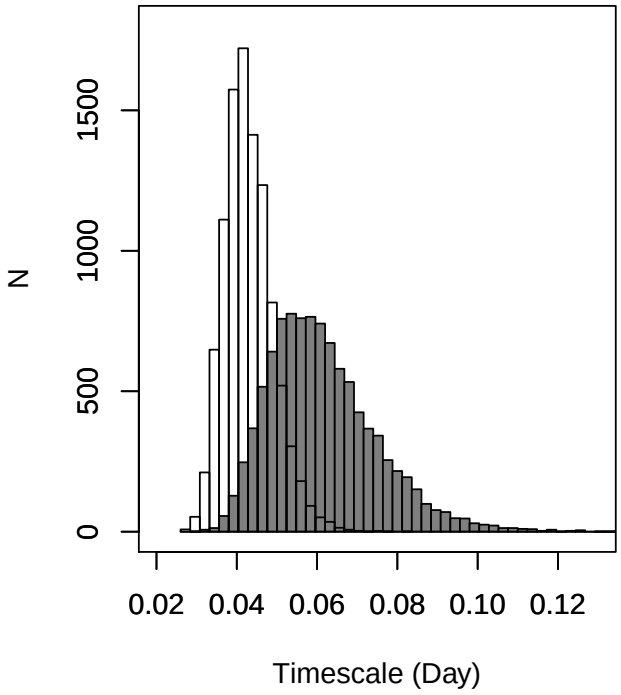

Fig. 6. Histograms of $T_{\rm r}$ (white) and $T_{\rm d}$ (gray) of the best-fit function (7). The best-fit parameters are calculated from 10^4 resampled mean profiles generated by the non-parametric bootstrap approach. See text for details.

Table 1. Parameters of best-fit function (7) to component 1 of the mean profile of shots

	Best-fit value
$T_{\rm r}$ (d)	0.043±0.001
$T_{\rm d}$ (d)	0.061±0.002
F_0 (count s^{-1})	76.7±0.6
$F_{\rm c}$ (count s^{-1})	1506.7±0.8

evaluations, component 1 in the mean profile is asymmetric in this case of 195 detected shot samples.

4.1.4 Amplitude Dependence of Mean Profiles

Since rapid variations observed in the light curve have various amplitudes, the shot detection is defined with a threshold of $>4\sigma$. If the profile of rapid variations depends on its amplitude, the calculated mean profile of shots does not reflect general features of the rapid variations. We separate detected shots into four groups based on amplitudes of 4–5.7σ, 5.7–7σ, 7–9.5σ, and over 9.5σ, and verify the

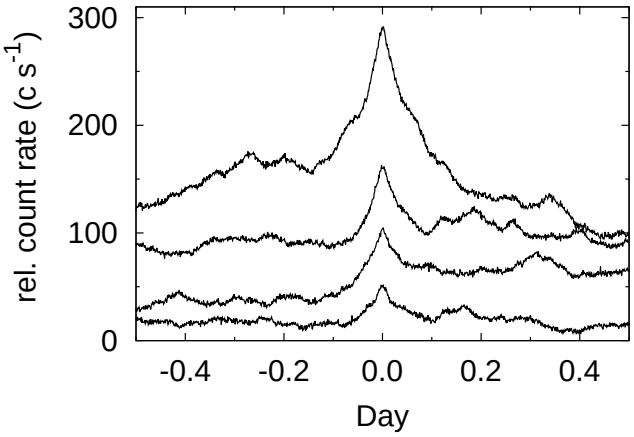

Fig. 7. Mean profiles of shots with different amplitudes. From bottom to top, profiles are calculated from shots with amplitudes of 4–5.7, 5.7–7, 7–9.5, and over 9.5σ, respectively. Each profile is offset for clarity. The vertical axis shows the relative count rate.

amplitude dependence of the shot profile by comparing the profiles of four groups. Figure 7 shows mean profiles of shots with different amplitudes. All profiles have the component 1 within $\pm$0.1 d of the center. These shot profiles do not have any clear trend associated with their amplitudes, except for the amplitudes of component 1, although these profiles have local features that are caused by the limited number of shot samples. All ratios of rise to decay timescales in each profile are less than unity (average and standard deviation of these ratios are 0.69$\pm$0.18). These results indicate that the mean profile of 195 shots reflects the general nature of the rapid variations, and the asymmetric feature of the mean profile of shots is not artificial one caused by the amplitude dependence of shots.

4.2 Shot Durations

Detected shots displayed a variety of shapes. It is, however, assumed that the averaged shape of shots converges to the exclusive shape in the shot analysis. If the averaged shape of shots converges to the unique shape which reflects the general feature of shots, durations of shots would distribute around its characteristic time. To validate the convergence of shot shapes, we calculate widths of e-folding rise and decay times in each shot as durations, and investigate its distribution.

We calculate the shot durations as follows: First, the baseline component under a shot is approximated by the second-order polynomial function. Here we set a fitting region for this approximation in each shot. Second, the approximated baseline component is subtracted from the light curve to estimate an amplitude of the shot. Thirds, e-folding timescales in a rise and decay phases are calculated from the subtracted light curve. Finally, these timescales are summed as a duration of the shot. In some cases of shots, other variation components are contaminated to the shot components. The e-

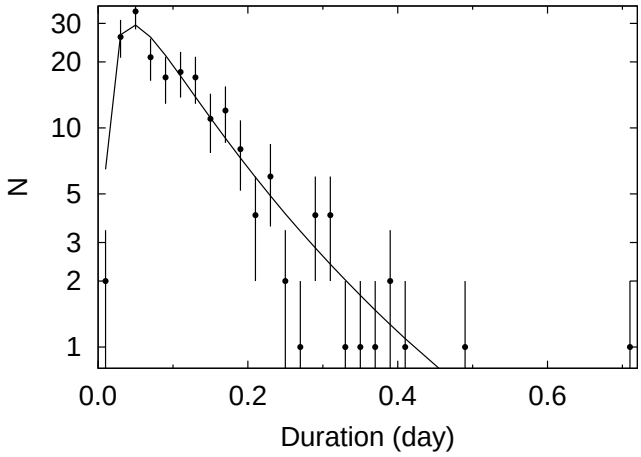

Fig. 8. Distribution of estimated shot durations. Solid line shows the best-fit log-normal distribution.

folding timescales should be longer for the contamination. Then, we extrapolate by linear regression to expect the buried shot component and estimate the e-folding time from the expectation.

4.2.1 Distribution of Durations

Figure 8 shows a distribution of shot e-folding durations. Estimated durations of shots are ranged from 0.018 to 0.71 d, with a mean of 0.122 and a standard deviation of 0.097 d. In table 2, there are the number, peak date, amplitude, duration, and rise and decay times in each shot. The durations are distributed with a characteristic time, and its distribution can be represented by the log-normal function:

$$f(x) = \frac{1}{\sqrt{2\pi}}\exp\left[-\frac{(\log x - \log\mu)^2}{2\sigma^2}\right] \tag{8}$$

where μ and σ represent the mean and variance of the distribution (Negoro et al. 2002). The distribution is evaluated to the log-normal function by the Kolmogorov and Smirnov test (with a p value of 0.53). The best-fit log-normal function is shown as a solid line in figure 8.

The mean of these durations is slightly larger than the duration (best-fit $T_{\rm r}$ plus $T_{\rm d}$ of 0.104 d) of the mean profile of shots. This can be caused by the large-side tail of the distribution of durations as evidence that the median value of the distribution of 0.098 d is similar to the value of $T_{\rm r}$ plus $T_{\rm d}$ of the mean profile.

If the durations arise following to a random manner or a provability distribution of a power-law function, the distribution should be a flat or no-peak shapes. If the distribution of durations follows to the power-law function with a lower cutoff, there is a physical background for the lower cutoff of this distribution, because the minimum duration of 0.018 d is clearly larger than the cutoff caused by the time-resolution limit of several times of 0.00068 d (=1 min). Thus, the duration at the peak of the

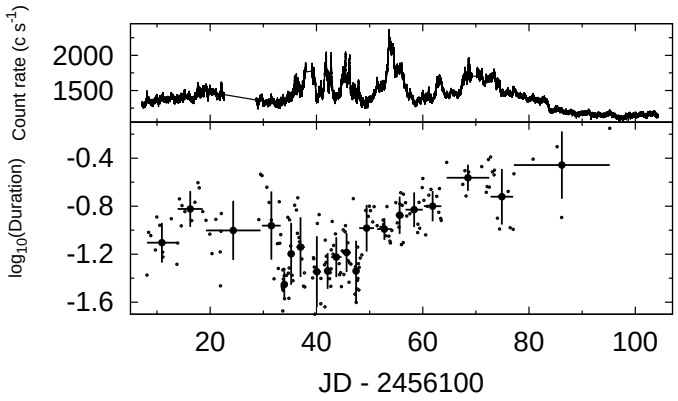

Fig. 9. Time series of shot durations. The *Kepler* light curve (upper panel) and the time variation of the durations are displayed. The time series of averaged durations is also shown in the bottom panel.

distribution is brought to the physics of the jet. Therefore, the distribution of the durations implies that the averaged shape of shots is converged to the typical one which reflects the physical background of the object.

4.2.2 Time Evolution of Variation Timescales

Figure 9 shows the light curve, and time series of estimated durations in the detected shots together with the average and standard deviation of each 10-points duration set in a logarithmic scale. The averaged durations show a systematic variation with time. To validate that this systematic variation is not a result of a random manner, we calculate a $\chi^2/\mathrm{d.o.f}$ of these averaged durations to the best-fit constant value in the logarithmic scale. Here, we assume that durations in each 10-point set are randomly distributed according to a log-normal probability density. Therefore, the standard deviation of each 10-point duration set is used as the $\sigma_{\rm err}$ in equation 1. The calculated $\chi^2/\mathrm{d.o.f}$ is equal to 52.3/19, which corresponds to a p value of 1.04×10^{-5}. This result indicates that the averaged durations are variable with time. Thus, the shot events are associated with each other, not randomly distributed.

4.3 Validation of Shot Features by Monte-Carlo Simulation

In §4.1, we found general features of rapid variation in the object by applying shot analysis to the *Kepler* light curve. It is not known, however, whether the general features result from the natures of the AGN jet physics or statistics. The observed general features extracted from the mean profile of shots should be separated into these two categories by using the Monte-Carlo method. We evaluate the stochastic features of the simulated noise variation generated by the Monte-Carlo method (see

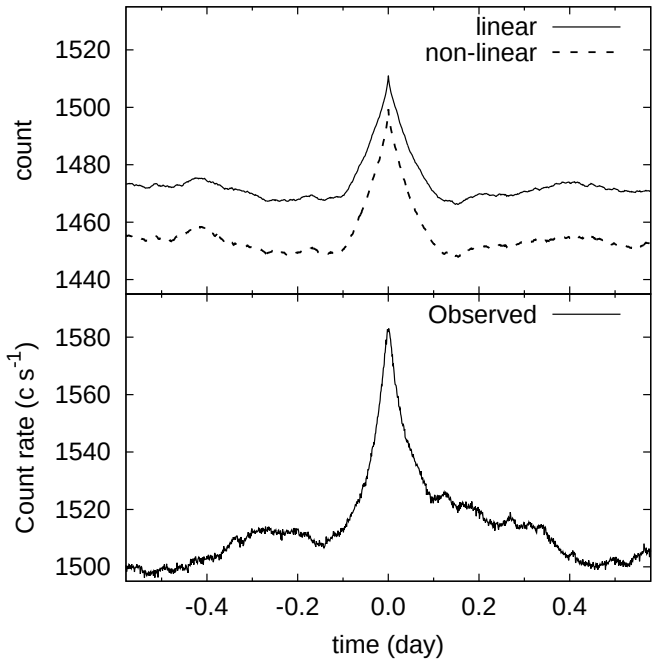

Fig. 10. Mean profiles of local peaks calculated from simulated linear and non-linear variations, and the observed mean profile of shots. The mean profiles in the top panel are calculated from 195 local peaks selected from a simulated linear (solid line) and non-linear (dashed line) variations. The observed mean profile of shots in the bottom panel is shown for comparison.

§3.3) by applying the shot analysis, and compare these features with the observed ones. Then we determine the causes of the observed features.

Figure 10 shows the mean profiles of local peaks selecting from simulated linear and non-linear variations, and displays the observed mean profile of shots for comparison. All profiles clearly have peak signals distributed about the origin. The rise and decay phases of the mean profiles calculated from both the simulated linear and non-linear variations are consistent with the exponential rise and decay forms, which are also consistent with the observed ones. Durations of the peak component in the mean profiles of local peaks in the linear and non-linear variations are approximately equal to the duration of component 1 ($\pm$0.1 d). This similarity can be caused by having the observed and reference PSDs having the same break frequencies, equal to 4.1×10^{-5} Hz.

Averages of e-folding times in the rise and decay phases of profiles calculated from the simulated linear and non-linear variations are approximately equal to 0.084 (rise in linear), 0.084 (decay in linear) 0.078 (rise in non-linear) and 0.078 d (decay in non-linear), respectively. Standard deviations of rise and decay e-folding times calculated from 10^3 simulated linear and non-linear variations are almost the same value, 0.015 d. The timescales in both the linear and non-linear cases are longer than those of the observed mean profile. Furthermore, the rise and decay timescales of profiles of the

simulated variations are almost the same. That is, the profiles are symmetric, while component 1 of the observed mean profile contains some asymmetry.

We evaluate whether the observed asymmetry can be explained by fluctuations in the simulated rise and decay timescales of local-peak profiles calculated from linear and non-linear variations. First, we generate 10^3 mean profiles of local peaks of simulated variations with the linear and non-linear processes. Second, the ratio between the best-fit e-folding times of the rise and decay phases is estimated from each mean profile. Finally, we compare the probability distributions of those ratios calculated from the 10^3 simulated linear and non-linear variations with the observed ratio between the e-folding times of rise and decay phases. Figure 11 shows histograms of 10^3 ratios between the rise and decay timescales of mean profiles in the cases of both the linear and non-linear processes. These are clearly distributed about unity. This result indicates that the rise and decay timescales calculated from linear and non-linear noise variations should be the same. According to the Student's t-test, the ratio of timescales in the observed mean profile ($=0.70$) is clearly different with the median values of ratios calculated from these simulated mean profiles (the p values are both less than 2.2×10^{-16}). Thus, the difference between the rise and decay timescales observed in the mean profile of shots is caused by a physical phenomenon, not the result of the stochastic noise variation generated by the Monte-Carlo method using the PSD with a break frequency.

5 Discussion

5.1 Origin of rapid variations

It is poorly understood whether rapid variations of blazars are intrinsic phenomena or an apparent one caused by a geometrical effect, such as the precession of a jet axis. There are several models that explain flux variations as apparent rather than as caused by changes in the intrinsic luminosity. This can occur, for example, if the Doppler factor varies owing to changes in the viewing angle in a bent jet (Villata & Raiteri 1999) or to the effects of gravitational lensing (Chang & Refsdal 1979). Such models, however, predict that the averaged variation profile is approximately symmetric in a simple geometry, because the Doppler factor or lensing should change symmetrically. In other words, rise and decay timescales of an average profile of rapid variations should be roughly equal, whereas the estimated rise and decay timescales are different. Thus, rapid variations can not generally be explained by these models, but rather as intrinsic phenomena. If particles are accelerated in the jet, the number of higher-energy particles are increased in the emitting region during rapid variations, where they dissipate their energies. The flux-variation profile should be asymmetric in this particle-acceleration scenario, because the rise and decay of the brightness are caused by different mechanisms: particle

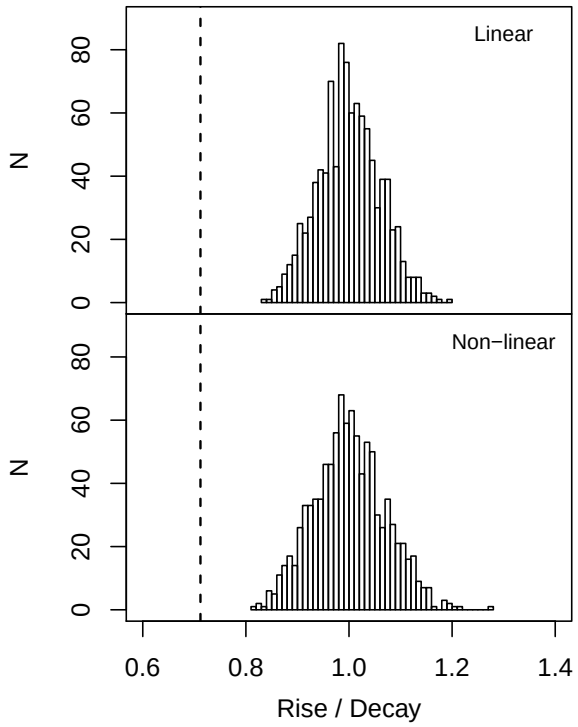

Fig. 11. Histograms of 10^3 ratios between rise and decay timescales. The rise and decay timescales are calculated as e-folding times of mean profiles of simulated linear (top panel) and non-linear (bottom panel) variations. Dashed lines show the observed ratio of rise and decay timescales.

acceleration and dissipation processes. Therefore, rapid variations are plausibly explained by such the particle-acceleration scenario.

5.2 Values of the magnetic field and Doppler factor

The mean profile of shots calculated by the shot analysis represents the variation with the characteristic timescale. This reflects an "averaged" situation of emitting regions of shots. We can estimate the common physical values of emitting regions from the mean profile of shots.

It is plausible that the dissipation of high-energy particles during rapid variation is caused by a synchrotron cooling. The timescale for this process, $\tau_{\rm syn}$, can be related to the decay timescale $T_{\rm d}$, $\tau_{\rm syn} = T_{\rm d}/(1+z)$. The synchrotron cooling timescale is calculated as

$$\tau_{\rm syn} \sim 3.2{\times}10^4\ B^{-3/2}\ E^{-1/2}\ \delta^{-1/2} \quad {\rm s}, \tag{9}$$

where B is the strength of magnetic field in Gauss, δ is the Doppler factor, and E is the energy of synchrotron photon in the observer's frame in eV (Tashiro et al. 1995; Sasada et al. 2010). We obtain the relation between B and δ from the equation (9) and the observed $T_{\rm d}$ of the mean profile of shots as:

$$\delta = 26.1\ B^{-3} \left(\frac{T_{\rm d}}{0.061\ {\rm d}} \right)^{-2}, \tag{10}$$

where we adopt E as the *Kepler*-observed energy, E=1.88 eV (central wavelength of the spectral response of the *Kepler* instrument, λ=6600Å; see (Koch et al. 2010; Van Cleve & Caldwell 2010)). The estimated value of $T_{\rm d}$ can be regarded as typical of rapid variations, because the timescale is calculated from the mean profile of shots. Thus, the relation between δ and B is typical of rapid variations in this object.

We calculate $\delta = 209$ assuming B as 0.5 G which is typical value of γ-ray detected BL Lac objects (Ghisellini et al. 2010). The average Lorentz factor among such BL Lac objects is estimated as $\Gamma = 6.1$, and most are viewed within 10° of the jet axis (Ajello et al. 2014). The Doppler factor δ is represented by the Lorentz factor and the viewing angle θ: $\delta = (\Gamma - \sqrt{\Gamma^2 - 1}\cos\theta)^{-1} = 5.7$, calculated for $\theta = 10°$. The Doppler factor calculated from the observed timescale is much larger than the typical of γ-ray detected BL Lac objects. If the Doppler factor is consistent with the typical, equal to 10, the magnetic field is approximately equal to 1.4 G, which is higher than the typical value of γ-ray detected BL Lac objects.

An alternative idea is that the high-energy accelerated particles are dissipated by escaping from the emitting region. The dissipation timescale corresponds to the size of the emitting region, R and the Doppler factor, $R \leq \delta c T_{\rm d}$. The average size of emission region should be smaller than 1.6×10^{15} cm calculated from the decay timescale of the mean profile of shots. This limitation of the size of emission region is much smaller than that using in the multi-wavelength spectral study, roughly equal to 10^{17} cm.

5.3 Shape of the profile of rapid variations

Particle acceleration and energy loss processes can lead to an asymmetric profile of rapid variations. There are several proposed particle acceleration mechanisms in blazar jets, for example, the shock-in-jet scenario (Marscher & Gear 1985), and magnetic reconnections (Giannios et al. 2009). The mean profile reflects the general features of variations without local features associated with different physical situations at individual variations. Here we compare component 1 with a simulated time evolution of emission proposed by past papers.

A numerical approach for reconstructing an episode of blazar variability has been attempted to reproduce observed synchrotron light curves and multi-wavelength spectra (Kirk, Rieger & Mastichiadis 1998). Spada et al. (2001) suggest that the observed variability can be explained via the inverse Compton process within the internal shock scenario. They proceed by simulating the birth, propagation and collision of shells, calculating the spectrum produced in each collision, and

summing the locally produced spectra.

Kirk, Rieger & Mastichiadis (1998) calculate a simulated light curve of blazar variation assuming a model in which particles are accelerated at a shock front and cool by synchrotron radiation in the homogeneous magnetic field. In this model, the increase of the injection rate of accelerated high-energy particles is constant in time. The flux of synchrotron radiation from the shocked region varies depending on the balance between the acceleration and dissipation rates of high-energy electrons. The observed sharp peak of the mean profile of shots indicates that the dominant rate changes dramatically at the peak. Simulated light curves at the maximum frequency of the synchrotron SED (10^{18} Hz) and at a lower frequency (10^{16} Hz) are different. The peak shape of the simulated light curve at 10^{16} Hz is more spiky than that in 10^{18} Hz. Component 1 in the observed mean profile is similar to the case of 10^{16} Hz. Based on the model in Kirk, Rieger & Mastichiadis (1998), the sharply peak of the mean profile of shots implies that the synchrotron-peak frequency of the rapid variation can be higher than the *Kepler*-observed wavelength. The observed peak frequency of synchrotron SED is, however, below 10^{13} Hz (Edelson et al. 2013). Therefore, higher-energy electrons, which emit at higher frequencies of the synchrotron spectrum, could be generated during the rapid variation, whereas electrons emitting the more stable synchrotron spectrum are produced less sporadically.

Several authors assume that the injection rate is a function of the Lorentz factor of the accelerated particles (Kusunose, Takahara & Li 2000; Böttcher & Dermer 2010). The simulated flux with a constant injection rate of high-energy particles rises rapidly at the beginning of the injection, after which it rises more slowly. This feature is caused by a balance between the injection and dissipation rates of accelerated high-energy particles. The rising phase of the observed mean profile, however, follows a simple exponential increase. Therefore, the observed light curve in the rising phase does not correspond to that expected for a constant injection rate.

5.4 Implication for Systematic Variation of Shot Durations

The durations of detected shots changed both randomly and systematically through time. If the flux variation is caused by the high-energy electron acceleration to the relativistic speed, the obtained systematic change of shot durations implies that these acceleration events are correlated with each other. Several models are proposed for the mechanisms of particle acceleration in blazar jets, for example, the shock-in-jet scenario (Marscher & Gear 1985), and magnetic reconnections (Giannios et al. 2009). The particle acceleration event is, however, expected to happen randomly based on simple situations of proposed models. In the shock-in-jet model, the particle acceleration is provided by a shock wave arising from a collision of two dense plasmas. Similarly, shocks and particle accelerations

can occur in a field with two magnetic field lines of opposite polarity in the magnetic reconnection model. The generated shocks should not be associated with each other in both models.

Recently, several papers (Marscher 2014; Nalewajko et al. 2011) suggest that particle acceleration takes place in the jet flow of a blazar. Emissions from the accelerated particles are Doppler boosted by the speeds of the shock and jet flow. In a shock region where a particle acceleration arises, its speed and angle between the moving direction and our line of sight in the jet rest frame are determined with statistically random variations. Seen in bottom panel of figure 9, there are two types of variations. One is the systematic variation caused by the jet flow, the speed of which is almost constant. The other is the statistical variation which is caused by the random speed and the ejected angle of individual shocks. If the jet flow changes geometrically, the observed systematic behavior of the shot durations can be explained either due to the change in δ (caused by the change of the angle between the jet flow and our line of sight by the precession of the jet) or due to the change of the speed of the shock-generated active region. The averaged shot durations varied by almost a factor of ten. This difference is not a result of the statistical variations of individual shots, because the statistical randomness is diluted by the average of 10 durations. To evaluate this fraction of the variation, we estimate the difference of the viewing angle θ assuming that the bulk Lorentz factor Γ is constant with time. The angle θ changes from 0° to 29° for the variation of the averaged durations with a factor of ten, assuming Γ of 6.1. This difference of the viewing angle is almost three times larger than that of BL Lac objects (Ajello et al. 2014). If the difference of the viewing angle is less than 10°, the Γ should be larger than 18.

5.5 Comparison with Cygnus X-1

The existence of flare-like variations has long been known in stellar-mass black holes, such as Cygnus X-1 in the low/hard state, since the pioneering work by Oda et al. (1971). Negoro et al. (1994) firstly applied the superposed shot technique to Cygnus X-1 during its low/hard state, finding that (1) the average shot at soft X-ray bands has a rather time-symmetric profile, (2) the profiles are well described by a sum of exponential functions with time constants of $\sim$0.1 s and $\sim$1 s both in the rise and decay phases, and (3) the shots in the rise phase possess a soft energy spectrum, and rapidly harden as the intensity peaks, resulting in hard X-ray time lags (Miyamoto et al. 1993, and see also Negoro et al. 2001). Since there are apparent similarities between the shot properties of W2R 1926+42 and those of Cygnus X-1, it may be interesting to compare them, although the main radiation mechanisms may differ. (In the case of Cygnus X-1, there is inverse Compton scattering radiation with seed photons from an optically thick disk; see, e.g., Makishima et al. 2000).

We first compare the timescales of shots by scaling these black hole masses. The spectrum of W2R 1926+42 in the optical and infrared bands contaminates the radiation of its host galaxy. The luminosity of the host galaxy of W2R 1926+42 in the $K_{\rm S}$ band is approximately $1.2\times10^{44}\,{\rm erg\,s^{-1}} = 10^{10.5}\,L_\odot$ (Edelson et al. 2013). The black hole mass of the blazar can then be estimated as $10^{7.8}\,M_\odot$ by applying the black hole mass-bulge mass relation (Marconi & Hunt 2003). In this estimation, we assume that the luminosity from the bulge dominates the observed luminosity of host galaxy. In comparison, the black hole mass of Cygnus X-1 is $\sim 15\,M_\odot$ (see (Orosz et al. 2011)). The duration of rapid variations of W2R 1926+42 is $\sim 2\,\tau_{\rm br}$ =7.8$\times10^3$ s, as estimated from the break frequency of its PSD. This timescale can be scaled to 0.01 s if we assume a mass ratio of $10^{-6.6}$ and a Doppler factor of $\delta = 5.7$ (see §5.2). This scaled timescale is ten times shorter than that of shots seen in the black hole X-ray binary Cygnus X-1. The mean profiles of the hard X-ray shots are, however, similar, including the asymmetries.

We finally note that the presence of two timescales in the shots of Cygnus X-1 indicates the involvement of (at least) two processes: one related to rapid heating and another to motion of accreting material (Manmoto et al. 1996; Negoro et al. 2001). In fact, the timescale of $\sim$1 s is too long to explain by a local phenomenon near the black hole. If the similarity holds, long-term variations of the shots of W2R 1926+42 may partly be related to time variations in the underlying gas accretion flow that causes the launch of the jets.

We next examine the spectral variations. Asymmetry in the mean profile of the shots of Cygnus X-1 is more noticeable in the hard-X-ray band ranging from 100 to 200 keV (Yamada et al. 2013), which is apparently similar to the rapid variations observed in W2R 1926+42. Additionally, we note again that the shot profile of Cygnus X-1 contains soft rise and hard decay features. The shock acceleration scenario may possibly explain some features of the observed flux and spectral variations of the shots. If accelerated particles with a given maximum energy emit hard X-ray photons up to $\sim$200 keV, these particles could be produced rapidly in the shock, resulting in the rapid spectral hardening near the peak intensity. A numerical simulation by Machida & Matsumoto (2003) showed that particle acceleration near the time of peak flux in Cygnus X-1 was produced by magnetic reconnection. Kirk, Rieger & Mastichiadis (1998) also produced a similar soft-rise and hard-decay behavior at the frequency of the maximum in the synchrotron SED in a numerical simulation of shock acceleration. In stellar black hole binaries, it is also known that optical lags X-rays variations (e.g., Spruit & Kanbach 2002; Gandhi et al. 2010). Thus, spectral changes when shots appear at various wavelengths are very important to compare observable features of these shots and investigate their origin.

6 Conclusion

We have obtained a continuous optical light curve of the blazar W2R 1926+42 with 1-min time resolution with the *Kepler* spacecraft. The object exhibits violent variability and many rapid variations with timescales of hours.

The power spectrum density (PSD) calculated from the observed light curve cannot be represented a simple power-law function, but instead by a function that combines a power law with a squared Lorentzian function. The best-fit function indicates that the PSD has a break frequency of $4.1^{+0.6}_{-0.5}\times10^{-5}$ Hz, which corresponds to 0.045$\pm$0.006 d.

We have detected 195 rapid variations that we describe as shots. The amplitude after subtracting long-term baseline components are four times larger than the noise level. Selected shots show a large diversity in its profiles. An averaged profile can be, however, assumed to converge with a universal one reflecting general features of shots, since the observed PSD has a curvature with the break frequency.

According to our shot analysis, the mean profile produced from detected shots shows several features;

- There are three components ranging $-$0.10—0.10 d (component 1), $-$0.50—$-$0.15 d (component 2), and 0.10—0.45 d (component 3) in the mean profile of the shots. Amplitudes of these components are larger than the systematic uncertainty estimated from six mean profiles calculated from different epochs of the light curve.
- Component 1 possesses an asymmetric profile, with a faster rise than decay and with spiky but smoothly connected behavior near the peak. This asymmetry should be caused by the AGN jet physics, not the result of stochastic process, because the mean profile of local peaks at simulated noise variation calculated by the Monte-Carlo method can not explain the asymmetry.
- Representation by an exponential rise and decay function is better than that of another, often used function. E-folding times of the rise and decay are 0.043$\pm$0.001 d and 0.061$\pm$0.002 d, respectively.
- The timescale estimated from the break frequency shown in the observed PSD is consistent with the average of the rise and decay e-folding times of component 1 at the 1-sigma confidence level.
- The decay phase of the observed mean profile of shots can be represented by a simulated light curve based on the shock-in-jet scenario. In contrast, the rise phase of the observed mean profile is fit by an exponential function rather than by alternative functions inferred from past studies with numerical simulations.

Durations of the detected shots show a systematic variation with almost a factor of ten during the monitoring. This systematic variation indicates that the shots arise associated with each other.

The shot analysis is also feasible for studying the spectral nature of the variations, because of the large signal-to-noise ratio. Unfortunately, *Kepler* performed only one-band monitoring. Spectral and other additional observational studies are needed to completely understand the mechanism of rapid variations. Additionally, stochastic time-domain analyses, for example ARMA-type models, can be applied to the unprecedented high-quality and uniformly sampled data provided by *Kepler*.

Acknowledgments

The authors thank A. Marscher for valuable comments and language editing, and thank the referee for valuable comments. This work was supported by Grant-in-Aid for JSPS Fellow (No. 24.1447). MS is supported by the JSPS Postdoctral Fellowship for Research Abroad.

References

Abdo, A. A., et al. 2010, ApJ, 722, 520

Abdo, A. A., et al. 2011, ApJL, 733, L26

Ackermann, M., et al. 2016, ApJL, 824, L20

Aharonian, F., et al. 2007, ApJL, 664, L71

Ajello, M., et al. 2014, ApJ, 780, 73

Antonucci, R. 1993, ARA&A, 31, 473

Blandford, R. D. & Königl, A. 1979, ApJ, 232, 34

Borucki, W., et al. 2010, Sci, 327, 977

Böttcher, M., & Dermer, C. D. 2010, ApJ, 711, 445

Carini, M., Miller, H. R., & Goodrich, B. D. 1990, AJ, 100, 347

Chang, K., & Refsdal, S. 1979, Nature, 282, 561

Edelson, R., & Malkan, M. 2012, ApJ, 751, 52

Edelson, R., et al. 2013, ApJ, 766, 16

Efron, B. 1979 Ann. Stat., 7, 1

Efron, B., & Tibshirani, R. 1994, An Introduction to the Bootstrap (New York: Chapman & Hall CRC Monographs on Statistics & Applied Probability; Taylor and Francis

Gandhi, P., et al. 2010, MNRAS, 407, 2166

Ghisellini, G., et al. 2010, MNRAS, 402, 497

Giannios, D., Uzdensky, D. A., & Begelman, M. C. 2009, MNRAS, 395, L29

Jenkins, J., et al. 2010, ApJL, 713, L87

Kataoka, J., et al. 2001, ApJ, 560, 659

Kirk, J. G., Rieger, F. M., & Mastichiadis, A. 1998, A&A, 333, 452

Koch, D. G., et al. 2010, ApJ, 713, L79

Kusunose, M., Takahara, F., & Li, H. 2000, ApJ, 536, 299

Machida, M., & Matsumoto, R. 2003, ApJ, 585, 429

Makishima, K., et al. 2000, ApJ, 535, 632

Manmoto, T., Takeuchi, M., Mineshige, S., Matsumoto, R., Negoro, H. 1996, ApJL, 464, L135

Mann, H. B., & Whitney, D. R. 1947, Annals of Mathematical Statistics, 18, 50

Marconi, A., & Hunt, L. K. 2003, ApJL, 589, L21

Marscher, A. P., & Gear, W. K. 1985, ApJ, 298, 114

Marscher, A. P. 2014, ApJ 780, 87

Miyamoto, S., Iga, S., Kitamoto, S., & Kamado, Y. 1993, ApJL, 403, L39

Mohan, P., Gupta, A. C., Bachev, R., & Strigachev, A. 2016, MNRAS, 456, 654

Nalewajko, K., Niannios, D., Begelman, M. C., Uzdensky, D. A., & Sikora, M. 2011, MNRAS 413, 333

Nalewajko, K. 2013, MNRAS, 430, 1324

Negoro, H., Miyamoto, S., & Kitamoto, S. 1994, ApJL, 423, L127

Negoro, H., Kitamoto, S., & Mineshige, S. 2001, ApJ, 554, 528

Negoro, H., & Mineshige, S. 2002, PASJ, 54, L69

Oda, M., Gorenstein, P., Gursky, H., Kellogg, E., Schreier, E., Tananbaum, H., & Giacconi, R. 1971, ApJL, 166, L1

Orosz, J. A., McClintock, J. E., Aufdenberg, J. P., Remillard, R. A., Reid, M. J., Narayan, R., & Gou, L. 2011, ApJ, 742, 84

Papadakis, I. E., & Lawrence, A. 1993, MNRAS, 261, 612

Quirrenbach, A., et al. 1992, A&A, 258, 279

Sasada, M., et al. 2008, PASJ, 60, 37

Sasada, M., et al. 2010, PASJ, 62, 645

Saito, S., Stawarz, Ł., Tanaka, Y. T., Takahashi, T., Madejski, G., & D'Ammando, F. 2013, ApJL, 766, L11

Spada, M., Ghisellini, G., Lazzati, D., & Celotti, A. 2001, MNRAS, 325, 1559

Spruit, H. C., & Kanbach, G. 2002, A&A, 391, 225

Tashiro, M., et al. 1995, PASJ, 47, 131

Timmer, J., & König, M. 1995, A&A, 300, 70

Uttley, P., McHardy, I. M., & Vaughan, S., 2005, MNRAS, 359, 345

Van Cleve, J., & Caldwell, D. 2010, Kepler Instrument Handbook, KSCI-10933-001, NASA Ames Research Center, Moffett Field, CA (http://keplergo.arc.nasa.gov/Instrumentation.shtml)

Villata, M., & Raiteri, C., M. 1999, A&A, 347, 30

Wilcoxon, F. 1945, Biometrics Bulletin, 1, 80

Yamada, S., Negoro, H., Torii, S., Noda, H., Mineshige, S., & Makishima, K. 2013, ApJ, 767, L34

Table 2. Amplitude and

E-folding Timescales of Shots

No	Date	Amplitude	Duration	Rise Time	Decay Time
1	8.0924	152±17	0.042±0.006	0.018±0.005	0.024±0.001
2	8.4207	82±17	0.096±0.035	0.057±0.017	0.039±0.018
3	8.8232	71±14	0.090±0.035	0.042±0.016	0.048±0.020
4	9.6917	69±14	0.068±0.034	0.039±0.019	0.029±0.015
5	9.9423	110±14	0.129±0.031	0.108±0.025	0.020±0.005
6	10.5070	96±20	0.110±0.039	0.040±0.019	0.069±0.020
7	11.0410	90±12	0.066±0.012	0.043±0.009	0.022±0.003
8	11.0976	92±12	0.060±0.010	0.016±0.004	0.043±0.005
9	12.6751	96±12	0.125±0.029	0.087±0.020	0.038±0.009
10	13.7452	78±13	0.052±0.016	0.008±0.002	0.044±0.014
11	13.8821	79±13	0.078±0.022	0.034±0.008	0.044±0.014
12	14.2036	118±13	0.182±0.025	0.077±0.011	0.105±0.014
13	14.5496	123±12	0.109±0.013	0.073±0.012	0.036±0.001
14	14.6940	120±12	0.160±0.012	0.082±0.004	0.078±0.008
15	15.2260	115±13	0.143±0.018	0.109±0.010	0.034±0.007
16	16.5085	69±14	0.120±0.040	0.054±0.020	0.066±0.020
17	17.1182	98±14	0.171±0.042	0.085±0.022	0.086±0.019
18	17.6801	245±25	0.249±0.018	0.149±0.006	0.100±0.012
19	17.9444	179±25	0.225±0.019	0.111±0.006	0.114±0.013
20	18.5908	145±17	0.143±0.017	0.060±0.005	0.083±0.013
21	19.2072	136±16	0.121±0.009	0.058±0.003	0.063±0.007
22	19.9265	101±16	0.093±0.028	0.043±0.008	0.050±0.020
23	20.3325	74±13	0.064±0.017	0.042±0.008	0.021±0.009
24	21.0640	118±13	0.123±0.040	0.046±0.005	0.077±0.035
25	21.8950	94±14	0.066±0.010	0.046±0.008	0.020±0.002
26	21.9277	93±14	0.034±0.014	0.003±0.002	0.032±0.012
27	22.0333	216±13	0.098±0.004	0.049±0.001	0.049±0.003
28	22.0905	229±13	0.138±0.006	0.042±0.002	0.096±0.003
29	29.1416	80±13	0.123±0.022	0.068±0.012	0.054±0.010
30	29.4686	181±17	0.293±0.025	0.203±0.016	0.090±0.009

Column 1 - Number, 2 - Peak MJD, 3 - Amplitude (c s^{-1}), 4 - Duration (d), 5 - Rise Time (d), 6 - Decay Time (d)

Table 2. Continue

No	Date	Amplitude	Duration	Rise Time	Decay Time
31	29.7492	197±16	0.285±0.023	0.122±0.010	0.164±0.013
32	30.6490	77±24	0.228±0.118	0.169±0.076	0.059±0.042
33	31.0815	111±14	0.170±0.032	0.086±0.015	0.084±0.017
34	31.5045	124±23	0.122±0.052	0.068±0.021	0.053±0.031
35	32.0017	69±14	0.039±0.017	0.020±0.011	0.020±0.006
36	32.6583	101±26	0.077±0.040	0.031±0.016	0.046±0.024
37	32.8293	91±13	0.048±0.013	0.034±0.008	0.014±0.006
38	32.9961	175±19	0.173±0.022	0.070±0.011	0.103±0.011
39	33.0929	141±19	0.078±0.011	0.035±0.005	0.043±0.006
40	33.2706	127±12	0.092±0.013	0.034±0.004	0.058±0.009
41	33.5451	98±16	0.034±0.007	0.024±0.003	0.010±0.004
42	33.6371	92±19	0.033±0.011	0.020±0.008	0.013±0.003
43	33.6623	115±19	0.021±0.004	0.012±0.002	0.010±0.002
44	33.6861	114±18	0.047±0.008	0.027±0.004	0.019±0.003
45	33.7175	126±18	0.031±0.007	0.019±0.006	0.012±0.000
46	33.7604	131±18	0.039±0.004	0.027±0.001	0.012±0.003
47	33.8646	94±13	0.047±0.010	0.017±0.006	0.030±0.004
48	33.9300	100±13	0.042±0.009	0.012±0.002	0.030±0.007
49	33.9926	74±13	0.027±0.005	0.019±0.003	0.008±0.002
50	34.3714	71±14	0.042±0.010	0.015±0.006	0.027±0.003
51	34.6043	158±17	0.128±0.006	0.077±0.005	0.051±0.011
52	34.7221	97±13	0.044±0.010	0.038±0.009	0.006±0.002
53	34.7977	85±14	0.027±0.004	0.013±0.003	0.014±0.001
54	34.8495	136±14	0.048±0.001	0.026±0.001	0.022±0.002
55	34.9490	119±15	0.122±0.020	0.052±0.008	0.070±0.012
56	35.1363	104±13	0.074±0.004	0.036±0.004	0.037±0.000
57	35.2146	103±13	0.063±0.009	0.030±0.002	0.033±0.006
58	35.4176	94±14	0.042±0.010	0.031±0.008	0.011±0.002
59	35.5763	118±13	0.038±0.013	0.014±0.004	0.024±0.009
60	35.8828	290±34	0.162±0.028	0.059±0.018	0.102±0.010

Table 2. Continue

No	Date	Amplitude	Duration	Rise Time	Decay Time
61	36.2247	307±26	0.147±0.014	0.104±0.010	0.044±0.003
62	36.4168	236±26	0.094±0.010	0.060±0.006	0.034±0.004
63	36.4835	248±26	0.186±0.016	0.041±0.004	0.145±0.012
64	36.7104	179±26	0.087±0.010	0.040±0.003	0.047±0.007
65	36.8282	141±26	0.080±0.019	0.051±0.012	0.029±0.007
66	37.2457	122±23	0.058±0.010	0.047±0.004	0.011±0.006
67	37.3888	139±25	0.074±0.019	0.028±0.008	0.046±0.010
68	37.5550	101±21	0.034±0.010	0.009±0.006	0.025±0.004
69	37.7532	110±13	0.044±0.007	0.035±0.007	0.009±0.000
70	37.7859	96±13	0.034±0.005	0.012±0.001	0.022±0.004
71	39.2837	116±12	0.040±0.006	0.015±0.002	0.024±0.003
72	39.4315	156±15	0.059±0.004	0.030±0.001	0.030±0.003
73	39.4771	186±15	0.058±0.004	0.036±0.003	0.022±0.001
74	39.5990	111±18	0.049±0.008	0.035±0.005	0.014±0.002
75	39.6883	73±19	0.020±0.007	0.004±0.002	0.015±0.005
76	40.1623	119±18	0.114±0.020	0.051±0.006	0.063±0.015
77	40.4975	108±15	0.135±0.028	0.051±0.011	0.084±0.017
78	40.7583	70±14	0.018±0.005	0.009±0.003	0.009±0.002
79	40.8040	72±15	0.024±0.002	0.018±0.001	0.007±0.001
80	40.8387	154±18	0.040±0.007	0.016±0.003	0.024±0.004
81	41.5171	159±13	0.051±0.005	0.022±0.002	0.030±0.002
82	41.5716	91±13	0.023±0.003	0.018±0.002	0.005±0.002
83	41.6608	172±35	0.083±0.020	0.044±0.012	0.039±0.008
84	41.7882	213±14	0.054±0.004	0.024±0.002	0.029±0.002
85	41.8590	256±14	0.061±0.009	0.040±0.007	0.021±0.002
86	42.0613	161±13	0.044±0.004	0.023±0.004	0.021±0.000
87	42.1219	177±13	0.048±0.000	0.032±0.001	0.016±0.001
88	42.4720	114±14	0.039±0.002	0.011±0.001	0.028±0.001
89	42.5769	130±15	0.044±0.009	0.028±0.004	0.016±0.005
90	42.6941	124±16	0.034±0.003	0.014±0.001	0.020±0.002

Table 2. Continue

No	Date	Amplitude	Duration	Rise Time	Decay Time
91	42.7636	388±33	0.048±0.004	0.029±0.002	0.019±0.002
92	42.7813	455±33	0.069±0.009	0.017±0.001	0.052±0.008
93	42.9631	192±23	0.118±0.014	0.038±0.004	0.081±0.010
94	43.1218	76±17	0.063±0.012	0.018±0.006	0.045±0.007
95	43.2397	126±17	0.075±0.011	0.026±0.005	0.049±0.006
96	43.5796	137±13	0.093±0.013	0.058±0.008	0.035±0.005
97	44.2791	125±12	0.053±0.006	0.036±0.006	0.017±0.000
98	44.3458	95±12	0.043±0.006	0.031±0.004	0.011±0.003
99	44.5379	103±25	0.044±0.011	0.024±0.007	0.020±0.004
100	44.6925	91±13	0.034±0.007	0.024±0.004	0.010±0.002
101	44.8451	160±16	0.067±0.008	0.034±0.005	0.033±0.003
102	45.0283	213±19	0.101±0.016	0.070±0.009	0.031±0.007
103	45.1584	113±18	0.043±0.018	0.020±0.013	0.022±0.004
104	45.3839	237±23	0.097±0.008	0.045±0.003	0.052±0.005
105	45.4656	380±23	0.109±0.002	0.043±0.001	0.066±0.001
106	45.8940	189±19	0.079±0.006	0.049±0.003	0.030±0.003
107	45.9533	158±19	0.056±0.007	0.031±0.004	0.025±0.003
108	46.1154	190±18	0.037±0.005	0.025±0.004	0.012±0.001
109	46.2414	221±15	0.053±0.001	0.014±0.000	0.039±0.000
110	46.4771	131±21	0.052±0.006	0.018±0.001	0.034±0.005
111	46.9239	186±22	0.183±0.026	0.070±0.008	0.113±0.017
112	47.2290	171±18	0.029±0.006	0.014±0.004	0.016±0.002
113	47.3346	118±15	0.050±0.003	0.010±0.002	0.039±0.001
114	47.4749	80±16	0.025±0.008	0.014±0.006	0.011±0.002
115	47.6330	129±21	0.032±0.007	0.013±0.003	0.019±0.003
116	47.7160	192±23	0.038±0.006	0.024±0.004	0.014±0.002
117	47.7419	175±23	0.072±0.010	0.035±0.005	0.037±0.005
118	47.7835	147±23	0.040±0.009	0.022±0.003	0.018±0.006
119	47.9074	210±18	0.053±0.004	0.024±0.002	0.028±0.002
120	47.9749	140±18	0.032±0.005	0.016±0.002	0.016±0.002

Table 2. Continue

No	Date	Amplitude	Duration	Rise Time	Decay Time
121	48.0355	149±18	0.049±0.006	0.030±0.003	0.019±0.003
122	48.2214	82±17	0.059±0.008	0.028±0.005	0.031±0.003
123	48.5402	85±13	0.062±0.011	0.035±0.005	0.027±0.006
124	49.2615	137±16	0.146±0.008	0.042±0.005	0.104±0.004
125	49.5306	162±17	0.102±0.015	0.057±0.007	0.045±0.008
126	49.7492	109±14	0.130±0.013	0.038±0.005	0.093±0.008
127	49.9624	119±15	0.159±0.006	0.093±0.001	0.065±0.005
128	50.1661	100±15	0.146±0.031	0.087±0.017	0.058±0.014
129	50.5918	88±16	0.117±0.027	0.062±0.021	0.055±0.006
130	50.8411	100±13	0.157±0.020	0.067±0.006	0.091±0.014
131	51.4016	120±16	0.109±0.015	0.043±0.008	0.066±0.008
132	52.1522	125±15	0.105±0.016	0.034±0.007	0.071±0.009
133	52.5371	134±18	0.121±0.018	0.073±0.012	0.048±0.006
134	52.6133	123±18	0.112±0.015	0.037±0.005	0.075±0.009
135	53.0431	129±16	0.090±0.010	0.040±0.006	0.050±0.004
136	53.2638	215±16	0.158±0.009	0.095±0.007	0.063±0.002
137	53.6228	235±28	0.089±0.007	0.038±0.003	0.051±0.004
138	53.8298	118±18	0.081±0.013	0.030±0.005	0.051±0.008
139	53.9136	104±18	0.078±0.006	0.025±0.000	0.053±0.006
140	54.1772	156±14	0.099±0.007	0.024±0.003	0.076±0.004
141	54.9360	170±16	0.170±0.010	0.078±0.005	0.092±0.004
142	55.1928	135±14	0.115±0.032	0.038±0.010	0.077±0.022
143	55.5170	122±18	0.106±0.013	0.050±0.008	0.056±0.005
144	55.6920	205±17	0.165±0.015	0.052±0.005	0.114±0.010
145	55.8432	221±17	0.205±0.016	0.102±0.008	0.104±0.008
146	55.9931	222±17	0.076±0.004	0.061±0.003	0.015±0.001
147	56.0367	227±17	0.130±0.010	0.071±0.005	0.059±0.004
148	56.1211	216±17	0.161±0.013	0.122±0.010	0.039±0.003
149	56.3207	150±17	0.079±0.010	0.055±0.007	0.024±0.003
150	56.3765	164±17	0.199±0.014	0.054±0.006	0.146±0.009

Table 2. Continue

No	Date	Amplitude	Duration	Rise Time	Decay Time
151	56.7662	102±14	0.169±0.023	0.147±0.013	0.023±0.010
152	56.9855	124±14	0.131±0.014	0.087±0.009	0.045±0.005
153	57.5746	103±14	0.137±0.024	0.067±0.010	0.070±0.013
154	58.0909	71±12	0.144±0.034	0.060±0.013	0.084±0.022
155	59.0322	99±13	0.096±0.010	0.078±0.009	0.018±0.000
156	59.0772	111±13	0.112±0.022	0.019±0.004	0.093±0.018
157	59.2849	116±13	0.171±0.018	0.115±0.017	0.056±0.000
158	59.4191	94±13	0.104±0.033	0.007±0.016	0.097±0.017
159	59.8871	166±12	0.226±0.020	0.144±0.014	0.082±0.006
160	60.0137	205±12	0.270±0.015	0.086±0.005	0.184±0.010
161	60.2160	134±12	0.177±0.018	0.095±0.008	0.083±0.009
162	60.5607	113±13	0.092±0.017	0.043±0.007	0.048±0.010
163	60.8897	88±12	0.158±0.033	0.107±0.026	0.051±0.008
164	61.1383	195±13	0.196±0.009	0.076±0.003	0.119±0.006
165	61.5469	124±17	0.219±0.028	0.138±0.008	0.081±0.019
166	62.6388	193±23	0.192±0.032	0.066±0.011	0.125±0.021
167	63.0045	126±17	0.141±0.021	0.072±0.016	0.069±0.006
168	63.1571	189±17	0.223±0.003	0.068±0.005	0.154±0.007
169	63.3805	146±17	0.125±0.024	0.074±0.014	0.051±0.010
170	63.4854	132±17	0.120±0.020	0.055±0.007	0.066±0.013
171	64.4955	111±15	0.367±0.074	0.079±0.020	0.288±0.054
172	67.5347	175±22	0.241±0.026	0.157±0.011	0.084±0.015
173	67.9290	293±20	0.313±0.022	0.137±0.010	0.176±0.012
174	68.1347	204±20	0.193±0.019	0.096±0.009	0.097±0.009
175	68.6238	351±20	0.306±0.016	0.098±0.009	0.208±0.007
176	71.0853	288±16	0.339±0.015	0.120±0.006	0.219±0.009
177	71.9496	188±15	0.207±0.021	0.107±0.013	0.100±0.008
178	72.1070	176±15	0.231±0.020	0.102±0.009	0.129±0.012
179	72.3651	189±16	0.388±0.032	0.269±0.021	0.119±0.010
180	72.5136	191±16	0.229±0.019	0.066±0.005	0.163±0.014

Table 2. Continue

No	Date	Amplitude	Duration	Rise Time	Decay Time
181	72.7595	241±16	0.408±0.027	0.181±0.012	0.226±0.015
182	73.1014	254±16	0.306±0.019	0.158±0.010	0.148±0.009
183	73.4229	295±15	0.289±0.016	0.238±0.013	0.051±0.003
184	73.4856	259±15	0.316±0.020	0.094±0.006	0.223±0.015
185	74.0488	110±14	0.126±0.015	0.062±0.007	0.064±0.008
186	74.4514	93±13	0.102±0.017	0.030±0.006	0.072±0.011
187	74.9990	87±13	0.185±0.039	0.080±0.016	0.106±0.023
188	76.0683	80±12	0.210±0.059	0.151±0.046	0.059±0.013
189	76.4395	75±13	0.105±0.031	0.063±0.022	0.042±0.010
190	77.0226	108±12	0.102±0.017	0.060±0.008	0.042±0.008
191	77.1561	100±12	0.295±0.057	0.105±0.032	0.190±0.025
192	80.7578	109±13	0.391±0.112	0.232±0.064	0.158±0.048
193	85.2674	87±13	0.497±0.137	0.230±0.079	0.267±0.058
194	86.1263	73±12	0.128±0.018	0.085±0.017	0.042±0.001
195	95.1884	95±14	0.706±0.317	0.275±0.127	0.431±0.191

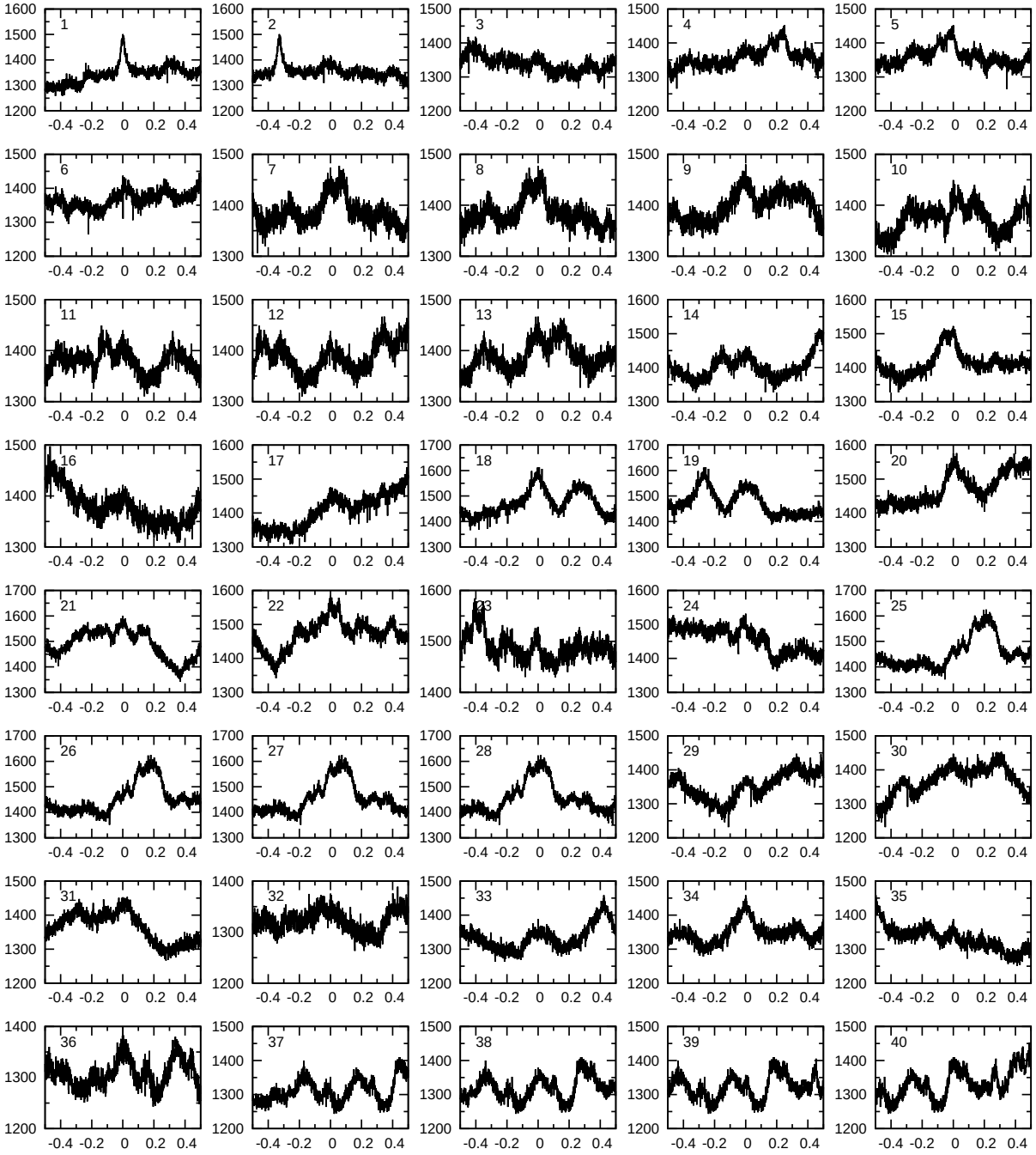

Fig. 12. Light curve of each detected shot obtained by the *Kepler* spacecraft over the entire Quarter 14 period. The object was monitored for 100 d with 1-minute time resolution. Each shot is numbered at the left top. The number of each shot is listed in table 2.

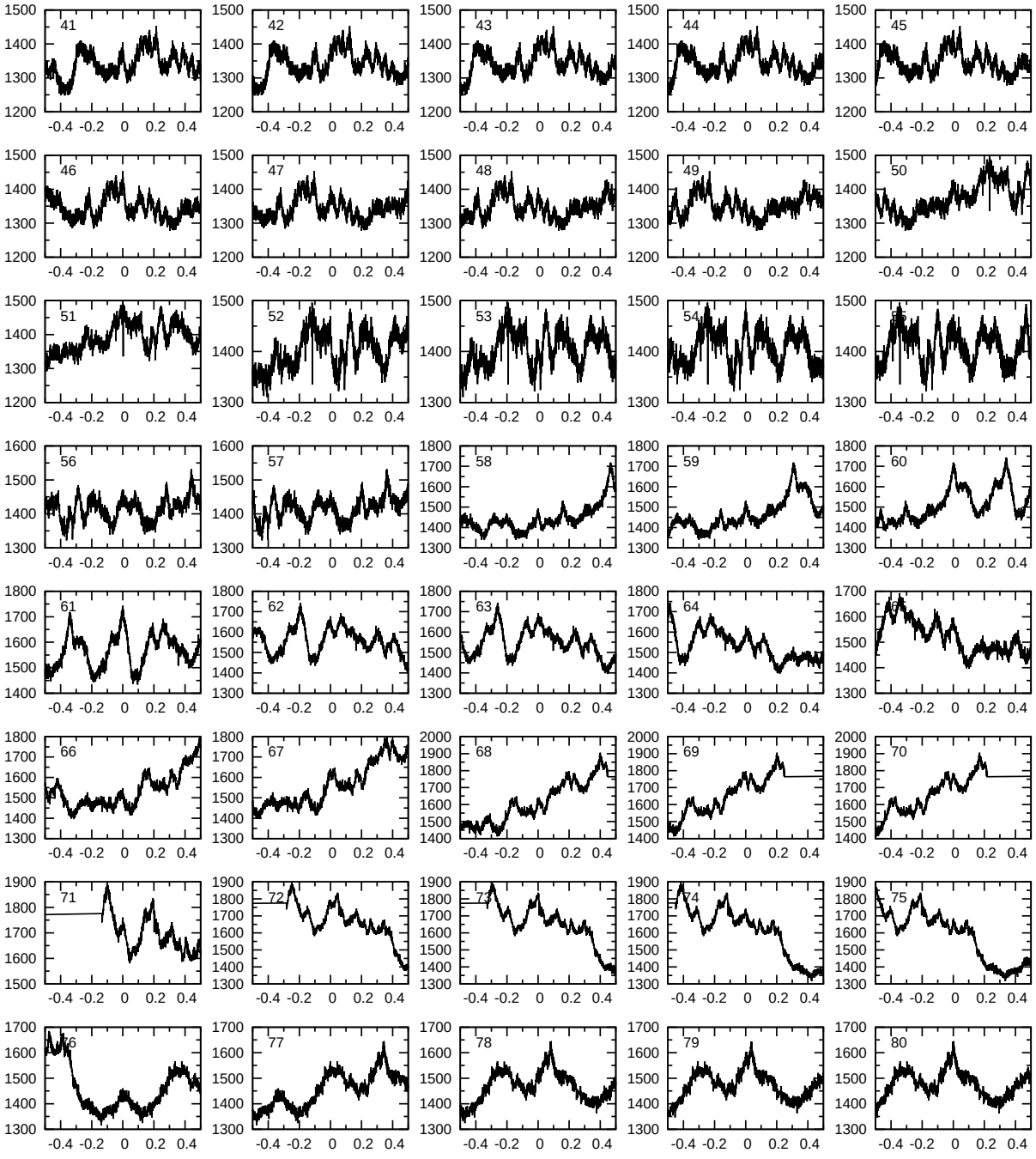

Fig. 12. (Continued)

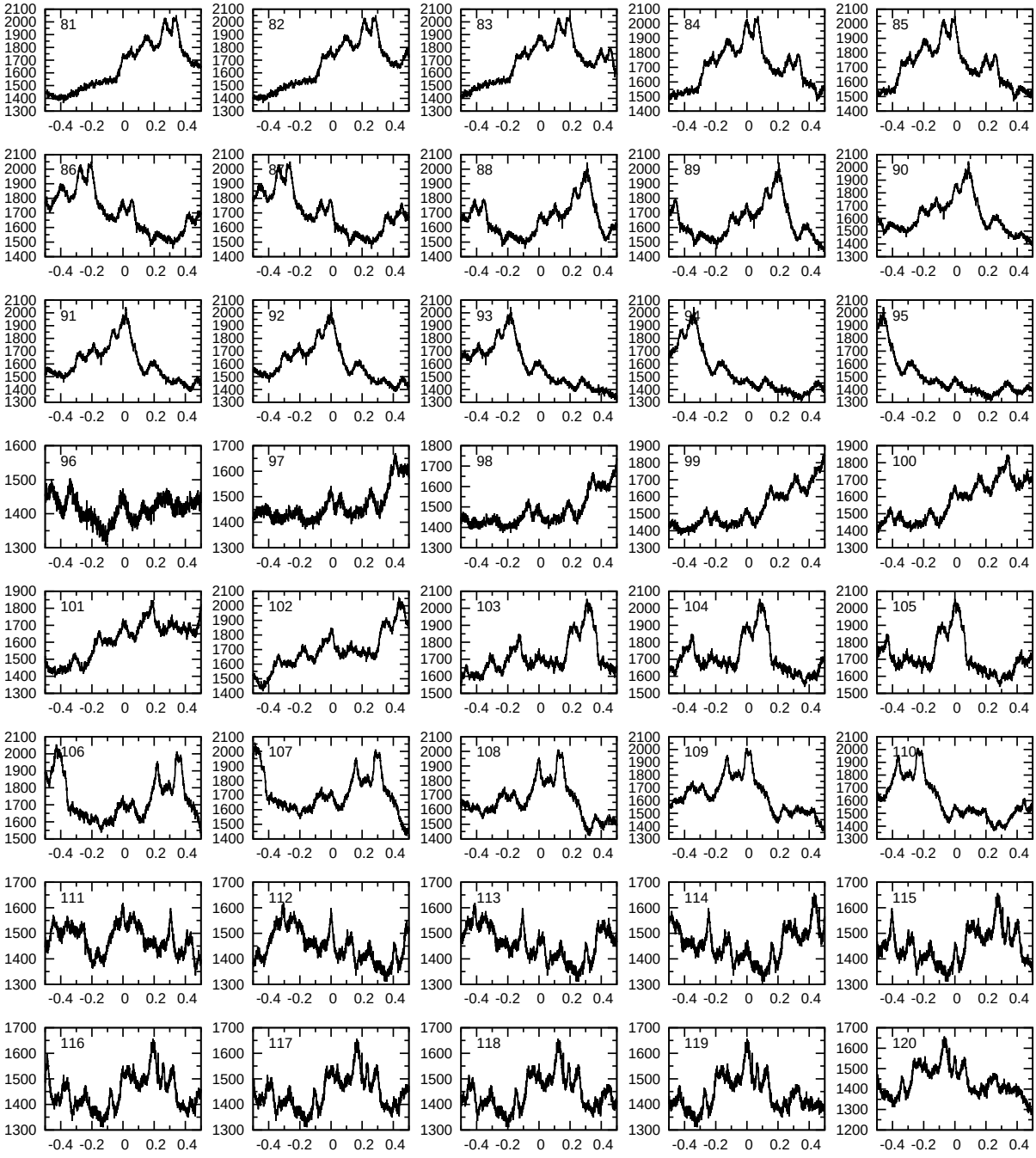

Fig. 12. (Continued)

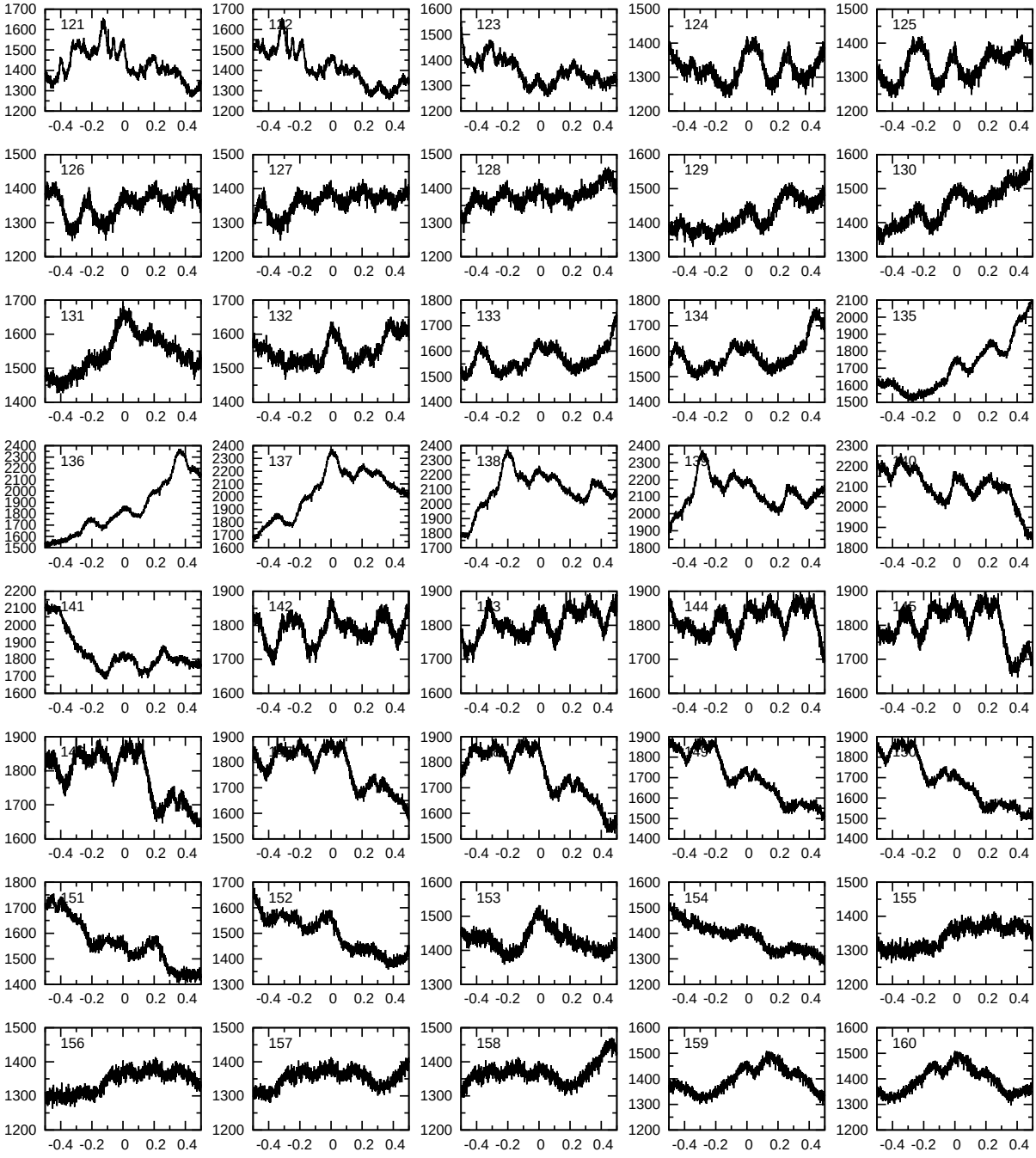

Fig. 12. (Continued)

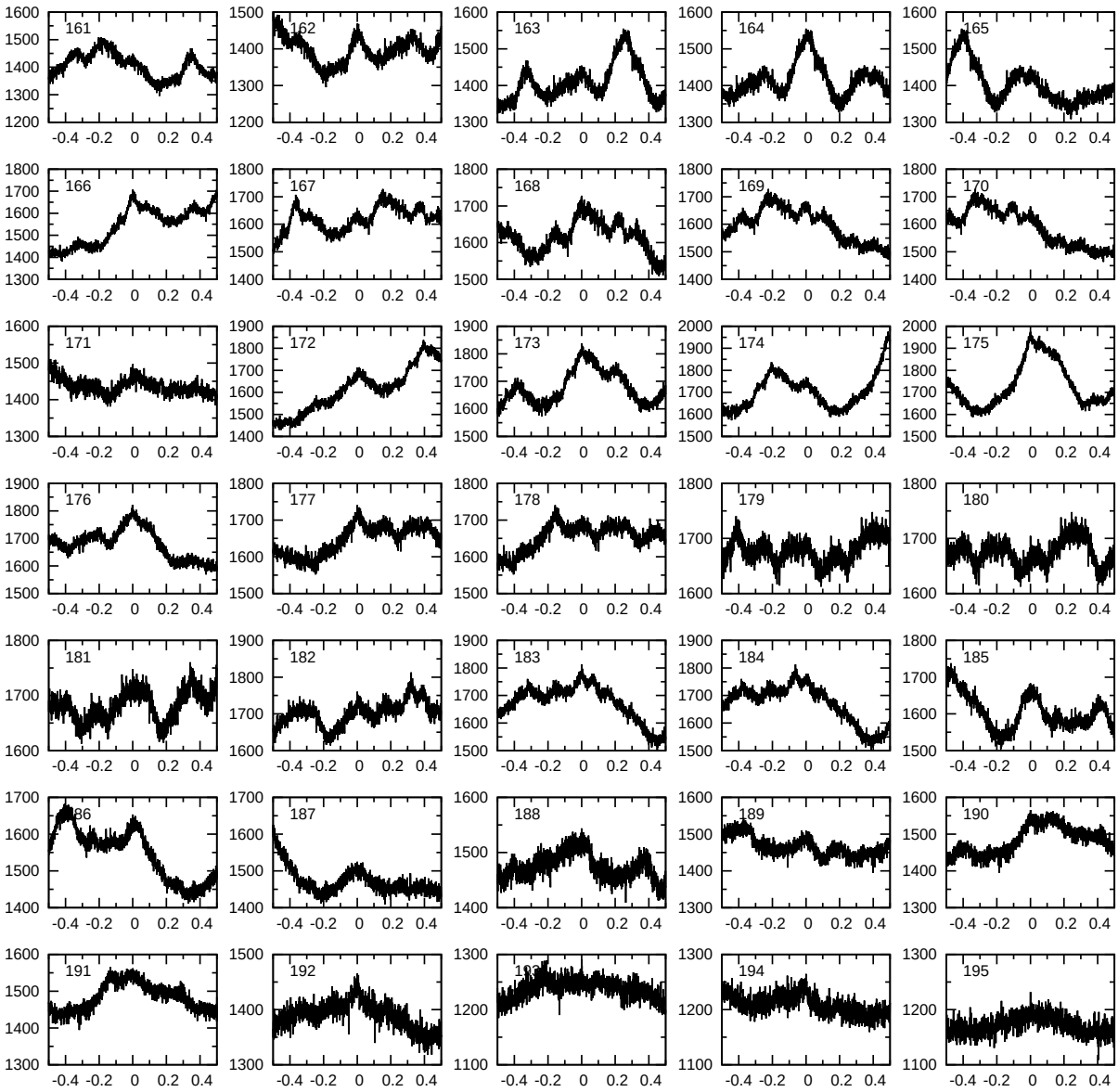

Fig. 12. (Continued)